Astronomy & Astrophysics manuscript no. aa56891-25
October 22, 2025

Unveiling the nature of HE 0107−5240: a long period binary CEMP-no star with [Fe/H] of –5.56 ⋆

E. Caffau[1,2], M. Steffen[3], P. Molaro[2,4], P. Bonifacio[1,2], N. Christlieb[5], D. S. Aguado[6,7], J. I. González Hernández[6,7], M. R. Zapatero Osorio[8], L. Monaco[9,2], M. Limongi[10,11,12], A. Chieffi[13,11,14], A. Falla[15,11], L. Roberti[16,11,17,18], A. J. Gallagher[19], M. Spite[1], P. François[1,20], H.-G. Ludwig[5], L. Sbordone[21], R. Lallement[1], C. Allende Prieto[6,7], R. Rebolo[6,7], S. Cristiani[2,4], G. Cupani[2,4], V. D'Odorico[2,4], C. J. A. P. Martins[22,23], D. Milaković[2,4], M. T. Murphy[24], N. J. Nunes[25], N. C. Santos[22,26], and T. M. Schmidt[27]

(Affiliations can be found after the references)

Received July 15, 2024; accepted August 16, 2024

ABSTRACT

ontext. The vast majority of the most iron-poor stars in the Galaxy exhibit a strong carbon enhancement, with C/H ratios only about two orders f magnitude below solar. This unusual chemical composition likely reflects the properties of the gas cloud from which these stars formed, having een enriched by one, or at most a few, supernovae. A remarkable member of this stellar class, HE 0107−5240 with [Fe/H]=–5.56, has been dentified as part of a binary system.

ims. To constrain its orbital parameters, radial velocity monitoring has been carried out using the ESPRESSO spectrograph.

ethods. Radial velocities were derived using cross-correlation with a template, taking advantage of the strong G-band feature. Combining ll observations yielded a high signal-to-noise spectrum, which has been used to refine our understanding of the stellar chemical composition. dditionally, a co-added UVES spectrum in the blue was used to complement the wavelength coverage of ESPRESSO.

esults. Observations of HE 0107−5240 over a span of more than four years have yielded a revised orbital period of about 29 years. Updated lemental abundances have been determined for Sc, Cr, Co, and, tentatively, Al, along with a new upper limit for Be. The iron abundance has been erived from ionised Fe lines. Significant upper limits have been established for Li, Si, and Sr.

onclusions. The star is confirmed to be a long-period binary. Iron abundances derived from neutral and ionised lines are consistent with local hermodynamical equilibrium (LTE) assumption, casting doubt on published deviation from LTE corrections for Fe for this star. The heavy lements Sr and Ba remain undetected, confirming the classification of HE 0107−5240 as a carbon enhanced metal-poor and non enhanced in eavy elements (CEMP-no) star and supporting the absence of an n-capture element plateau at the lowest metallicities.

ey words. Stars: abundances - Galaxy: abundances - Galaxy: evolution - Galaxy: formation

. Introduction

he metal-poor stars shining today in the sky are expected to ave formed shortly after the Big Bang from gas clouds that ere only slightly enriched by one or a few supernova exploions. Given their life times comparable to the age of the Uni-erse, they must have low masses ($M < 0.8 M_{\odot}$.) Metal-poor tars have been known since the early work of Chamberlain & ller (1951), but it was the HK survey by Beers et al. (1992) hat led to the discovery of a distinct group: carbon-enhanced, ron-poor stars. Within this group, a subclass was identified that ombines high carbon enhancement with a deficiency or absence f n-capture elements (Norris et al. 1997; Bonifacio et al. 1998). The star HE 0107−5240 was discovered at the beginning of this century (Christlieb et al. 2002) and has since become the prototype of this rare class, which now includes most of the most iron-poor stars known.

Currently, about a dozen stars are known with extremely low iron abundances ([Fe/H] < −4.5) and relatively high carbon abundances (5.5 < A(C) < 7.8). Only two known stars in this regime (SDSS J102915.14+172927.9 Caffau et al. 2011a and Pristine J221.8781+09.7844 Starkenburg et al. 2018) do not exhibit carbon enhancement, having only upper limits on their carbon abundances: A(C) < 4.68 for the former (Caffau et al. 2024b) and below 6.0 for the latter (Lardo et al. 2021). Recently Limberg et al. (2025), reported of an evolved star which shows no C in the spectrum and, after taking into account for the lost C into N, the upper limit is just A(C) < 4.79 ([C/Fe] < +1.18).

Un-evolved, warm stars ($T_{\rm eff}$> 5800 K) often display a weak G-band, making carbon abundance determinations challenging and complicating the identification of extremely metal poor stars, EMP, that are not carbon-enhanced (i.e., not CEMP, a CEMP being here defined as [C/Fe] > 1.0, Beers & Christlieb 2005). According to Bonifacio et al. (2015), CEMP-no stars show a relatively constant absolute carbon abundance, lower than that of CEMP-s stars, which also show enhanced abundances of s-process elements. The carbon in CEMP-s stars likely originates from mass transfer from an evolved asymptotic giant branch (AGB) companion, along with elements such as Sr and Ba. In contrast, the carbon in CEMP-no stars is likely primordial. The so-called 'low-carbon band' (Bonifacio et al. 2015) is centred around A(C) ∼ 6.8. We therefore suggest that in the ultra-iron-poor regime ([Fe/H] < −4.5), stars with A(C) > 5.8 should be classified as CEMP, rather than relying solely on [C/Fe] > 1.

It is plausible that carbon-normal and carbon-enhanced ultra iron-poor stars have distinct origins. For example, SDSS J102915.14+172927.9 exhibits a solar-scaled abundance

⋆ Based on ESPRESSO GTO observations collected under ESO programmes 0103.D-0700 and 108.2268.001 (PI: P. Molaro), 1104.C-0350 1102.C-0744 (PI F. Pepe), and 114.27NH.001 (PI: D. Aguado) pattern without the typical α-element enhancement seen in most metal-poor stars and an orbit in the Galactic disc. This may indicate that this is a Pop III star and that its stellar surface was polluted during its long journey through the Galactic disc (see Caffau et al. 2024b).

HE 0107−5240 was first reported by Christlieb et al. (2002), with a detailed chemical abundance analysis presented in Christlieb et al. (2004), based on UVES spectra. The oxygen abundance was later derived from OH molecular lines in the UV by Bessell et al. (2004). The impact of 3D hydrodynamic models on the inferred abundances was explored by Collet et al. (2006), while deviations from local thermodynamic equilibrium (NLTE) were examined for iron by Ezzeddine et al. (2017) and for Mg and Ca by Sitnova et al. (2019).

The star HE 0107−5240 was included in an ESO ESPRESSO GTO programme aimed at investigating binarity among the most metal-poor stars. Its binary nature was first suggested by Arentsen et al. (2019), who noted discrepancies between radial velocities measured with UVES and SALT. This was subsequently confirmed by Bonifacio et al. (2020) using early ESPRESSO data. Continued ESPRESSO monitoring over more than three years was analysed by Aguado et al. (2022), who derived a long orbital period of approximately 13,000 days (~36 years), showing that binary formation is not precluded at extremely low metallicities. Aguado et al. (2022) also measured a carbon isotopic ratio of $^{12}C/^{13}C = 87 \pm 6$. This value rules out mass transfer from an evolved AGB companion as the source of the observed carbon and implies a significant primordial production of ^{13}C in the progenitor. In the present study, we extend the temporal baseline of radial velocity monitoring and analyse a new, high signal-to-noise co-added spectrum derived from all the available ESPRESSO observations.

Table 1. Journal of the ESPRESSO observations with a measurement of the radial velocities.

Date	hour	MJD[a]	v_{rad} (km s^{-1})	error (km s^{-1})
2018-09-03	02:35:15.830	58364.1078	48.170	0.047
2019-08-03	07:31:54.524	58698.3138	47.925	0.014
2019-08-26	06:18:47.382	58721.2630	47.873	0.015
2019-09-04	04:57:33.171	58741.2506	47.905	0.016
2019-10-03	02:18:47.960	58759.0963	47.913	0.015
2020-12-07	02:19:17.802	59190.0967	47.741	0.017
2021-01-23	00:47:12.076	59435.1762	47.627	0.016
2021-08-09	05:16:11.004	59435.2195	47.647	0.013
2021-10-02	05:42:52.690	59489.2381	47.559	0.022
2021-10-31	01:28:39.476	59518.0615	47.593	0.014
2021-11-11	04:51:34.041	59529.2024	47.610	0.012
2022-01-27	01:00:20.859	59606.0419	47.525	0.020
2022-10-05	02:23:36.234	59857.0997	47.429	0.014
2022-10-06	05:15:07.307	59858.2188	47.408	0.014
2022-10-07	00:55:29.027	59859.0385	47.429	0.019
2022-10-09	01:55:47.567	59861.0804	47.446	0.017
2022-10-10	01:32:41.459	59862.0643	47.406	0.013
2022-10-13	06:35:05.896	59865.2743	47.496	0.018
2022-10-14	05:09:08.436	59866.2146	47.378	0.012
2022-10-15	06:16:20.113	59867.2613	47.383	0.013
2022-10-16	00:28:15.002	59868.0196	47.362	0.011
2022-10-17	01:28:38.559	59869.0615	47.411	0.018
2022-10-17	05:20:01.708	59869.2222	47.382	0.013
2022-10-30	00:36:16.959	59882.0251	47.391	0.015
2022-11-04	03:40:39.767	59887.1532	47.386	0.014
2022-11-10	03:37:47.954	59893.1512	47.437	0.012
2022-11-17	02:14:41.449	59900.0935	47.346	0.016
2022-11-22	02:34:23.004	59905.1072	47.395	0.012
2022-11-27	01:35:49.040	59910.0665	47.316	0.015
2022-12-02	01:18:39.614	59915.0546	47.350	0.020
2022-12-03	02:40:27.679	59916.1114	47.339	0.016
2022-12-04	01:01:41.885	59917.0428	47.381	0.012
2023-06-09	08:45:19.968	60104.3648	47.311	0.012
2024-10-04	01:12:31.436	60587.0503	46.841	0.017
2024-11-03	02:12:59.673	60617.0923	46.842	0.011
2024-12-03	03:02:13.415	60647.1265	46.857	0.010

Notes. [a] Modified Julian date at the start of observation.

2. Observations

HE 0107−5240 was observed as part of several ESPRESSO GTO programmes: 0103.D-0700, 108.2268.001, and 110.245W.001 (PI: P. Molaro); 1102.C-0744 and 1104.C-0350 (PI: F. Pepe); as well as during the open-time programme 114.27NH.001 (PI: D. S. Aguado). The observations were reduced all in the same way. The GTO data, previously analysed by Aguado et al. (2022) and Molaro et al. (2023), are here complemented with the additional open-time observations. All spectra cover the same wavelength range from 380 to 788 nm, and were corrected for the star's orbital motion, co-added, and used for a revised chemical abundance analysis.

Since the ESPRESSO spectrum extends only down to approximately 380 nm in the blue, UVES data were employed to study chemical species with transitions in the ultraviolet. The UVES spectra consist of a sequence of observations using the 346 nm setting, obtained between September 30 and December 27, 2002, for a total exposure time of 19.5 hours (see Bonifacio et al. 2021, for the observation log). A total of 22 observing blocks (OBs) from programme 70.D-0009 were available, of which 21 were usable (one OB was exposed for only 1 s and contained no signal). Most OBs had exposure times of 3600 s, with three exceptions at 1727, 1600, and 3960 s, respectively. The combined UVES spectrum reached a signal-to-noise ratio (S/N) of approximately 50 per pixel at 324 nm.

The individual UVES spectra were shifted to the rest frame, scaled relative to one another, and co-added using an iterative $\kappa\sigma$-clipping procedure to compute a weighted average while removing outliers. Due to the pixel scale of 0.215" per pixel in the blue arm of UVES, the resulting spectrum was oversampled; it was therefore rebinned by a factor of two. The final co-added spectrum achieves a peak S/N per 0.05 Å pixel of ~ 140 at 3800 Å, decreasing to S/N ~ 70 at 3350 Å and ~ 30 at 3100 Å.

The HRS at SALT spectrum (Arentsen et al. 2019) has been used only for the radial velocity determination.

3. Galactic Kinematics

We adopted coordinates, proper motions and parallax from Gaia DR3 (Gaia Collaboration et al. 2023), applying the parallax zero-point correction as prescribed by Lindegren et al. (2021). The distance derived from the parallax is of $6.93^{+1.1}_{-0.8}$ kpc. The star is part of a binary system, although the faint companion is not directly visible. Radial velocity variations have been extensively discussed by Aguado et al. (2022) and Molaro et al. (2023). For our analysis, we adopted the systemic (barycentric) radial velocity of the system, $V_{rad} = 46.6 \pm 0.1$ kms^{-1} (see Sec. 4), and used this value to derive the star's Galactic orbit.

Following the procedure described in Caffau et al. (2024a), we employed the galpy code (Bovy 2015) with the MWPotential2014 Galactic potential model. We integrated the orbit backward in time over 1 Gyr. For the solar motion, we adopted the parameters from Schönrich et al. (2010), assuming a solar distance to the Galactic centre of 8 kpc and a circular velocity of 220 kms^{-1} (Bovy et al. 2012).

The kinematical properties of the star are shown in Fig. 1. The upper and lower panels display its position in several diagnostic diagrams: the Toomre diagram (top-left), orbital energy

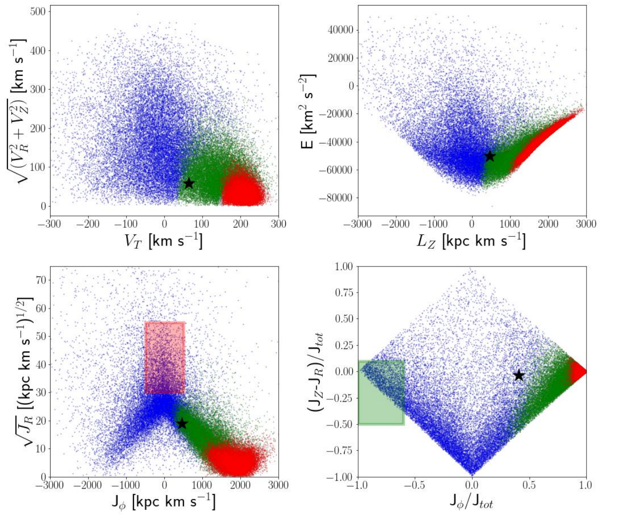

Fig. 1. Upper panels: HE 0107−5240 position (black filled star) in the Toomre diagram (left) and the orbital energy versus angular momentum (right). Bottom panels: square root of the radial action versus the azimuthal action (left) and action diamond (right). Coloured points are stars from the good-parallax sample of Bonifacio et al. (2021). The red and green shaded areas are the regions defined by Feuillet et al. (2021) to select candidate GSE and Sequoia stars.

versus angular momentum (top-right), the square root of the radial action versus the azimuthal action (bottom-left), and the action diamond (bottom-right). The star is marked with a filled black star symbol. For comparison, stars from the good-parallax sample of Bonifacio et al. (2021, coloured points) are also plotted. Based on the classification criteria of Bensby et al. (2014), thin disc, thick disc, and halo stars are shown in red, green, and blue, respectively. The red and green shaded boxes in the bottom panels correspond to the regions defined by Feuillet et al. (2021) for stars associated with the Gaia-Sausage-Enceladus (GSE, red box, bottom-left) and Sequoia (green box, bottom-right) accretion events.

Sestito et al. (2019) estimated a distance of 14.3 ± 1.0 kpc and classified the system as having a retrograde Galactic halo orbit with an apocentric radius of r_{ap} = 15.9 kpc. We adopt a significantly shorter distance of 6.93 kpc. According to the Bensby et al. (2014) criteria, the system is classified as a thick disc star, consistent with its location in the kinematic diagrams of Fig. 1. However, its vertical distance from the Galactic plane ($z = -6.2$ kpc), the maximum orbital height ($Z_{\rm max} \approx 6.3$ kpc), and its apocentric distance ($r_{\rm ap} = 9.9$ kpc) suggest otherwise. The orbit is eccentric ($e = 0.69$) and prograde, with positive angular momentum (L_Z) and transverse velocity (v_T). Moreover, the star does not appear to be associated with either the GSE or Sequoia structures.

We therefore conclude that HE 0107−5240 is best classified as a halo star on a prograde Galactic orbit.

4. Orbital parameters

We recomputed the orbital parameters of the binary star HE 0107−5240 considering the new measurements of radial velocities also for the observations of the first 3 years to benefit of a better template in the cross correlation analysis. The new measurements from ESPRESSO spectra are provided in Table 1. For the UVES and HRS at SALT spectra we used the measurements provided in Bonifacio et al. (2020) and Arentsen et al. (2019). For the HARPS spectrum we used that provided in Aguado et al. (2022). With respect to the epochs provided in Aguado et al. (2022)[1], we rejected a few measurements obtained from very low S/N spectra. The whole set of ESPRESSO radial velocities (RVs) follows a decreasing trend as expected for this long period binary. The $v_{\rm rad}$ data are binned in bins of 1−d to minimise the stellar jitter (see Fig. 2, upper-left panel). The RVs are modelled using the RADVEL code (Fulton et al. 2018)[2] including a Keplerian motion of the star plus an RV offset (the γ of the $v_{\rm rad}$ curve), and a jitter parameter for each instrument within a likelihood scheme implemented in python using CELERITE (Foreman-Mackey et al. 2017)[3].

The Keplerian orbit for radial velocity is described as:

$$v_{\rm rad} = \gamma + k_2(\cos(\nu_a + \omega) + e\cos(\omega)) \quad (1)$$

where the true anomaly ν_a is a function of the eccentric anomaly E, that is, in turn, a function of time, through Kepler's equation (see equations 1,2,3 in Fulton et al. 2018). The parameters that define the orbit are five: the orbital period (P_2), the orbital semi-amplitude velocity (k_2), the angle of periastron (ω), the eccentricity (e) and the time of passage at periastron ($T_{2,\rm peri}$). The RADVEL program allows to infer both the time of periastron, $T_{2,\rm peri}$, and the time at inferior conjunction of the star, $T_{2,\rm conj}$. An orbit can be fit using any set of independent parameters that can be derived from these five. Following Fulton et al. (2018), we chose to perform fitting and posterior sampling using the $\ln P_2$, $T_{2,\rm conj}$, $\sqrt{e}\cos\omega$, $\sqrt{e}\sin\omega$, $\ln k_2$ basis which helps to speed up the convergence. We chose $\ln k_2$ to avoid favouring large k_2 and $\ln P_2$ because P_2 may be long if compared with the observational baseline. The $v_{\rm rad}$ errors in the Fig. 2 include the jitter of each instrument and the $v_{\rm rad}$ offset has been subtracted. In addition, we adopted uniform priors for all parameters (see Table 2). The revised orbital period of the system is 28.9 ± 2 yr. One should be however aware that since the time during which we have been observing this system is shorter than the best-fit period, the actual uncertainty on the period could be larger than our estimate.

To sample the posterior distributions and obtain the Bayesian evidence of the model (that is, marginal likelihood, ln Z), we relied on nested sampling using DYNESTY (Speagle 2020)[4]. We initialised a number of live points equal to $N^3(N+1)$, to efficiently sample the parameter space, with $N = 10$ being the number of free parameters. In the middle panel of Fig. 2, we also show in grey a subsample of 300 models randomly selected from the final selection of ∼37,696 Bayesian samples from the posterior distributions. The binary mass function can be computed from the masses of the binary component (e.g. Tauris & van den Heuvel 2006), i.e. that of the seen star, M_2, and that of the unseen binary companion, M_1, and the orbital parameters as follows:

$$f(\mathrm{M}) = (M_1^3 \sin^3 i)/(M_1 + M_2)^2 \quad (2)$$

$$f(\mathrm{M}) = [(P_{\rm orb}k_2^3)/(2\pi G)](1 - e^2)^{3/2} \quad (3)$$

[1] Note that there is a typo in Table 2 of Aguado et al. (2022), the epoch 9618.061 is instead 9518.061.
[2] RADVEL is a Python package for modelling of radial velocity time series data, available in https://radvel.readthedocs.io/en/latest/index.html
[3] CELERITE is a library for fast and scalable Gaussian Process (GP) Regression in one dimension, available in https://celerite.readthedocs.io/en/stable/
[4] DYNESTY is a Pure Python, MIT-licensed Dynamic Nested Sampling package for estimating Bayesian posteriors and evidences, available in https://dynesty.readthedocs.io/en/stable/

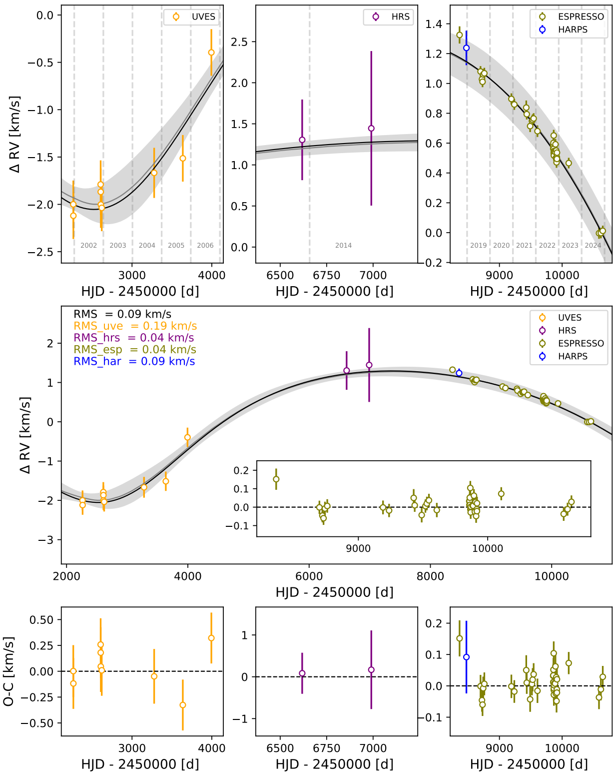

Fig. 2. Radial velocities (RV) of HE 0107−5240 versus heliocentric Julian date (HJD), together with the best RV model. The inner panel within the middle panel shows the ESPRESSO RV points after removing the best model. The RMS of the residuals of all RVs are provided within the middle panel and those from each spectrograph are given in the bottom panels.

With the Bayesian samples we computed the posterior distribution of the binary mass function providing the following result:

$$f(\mathrm{M}) = 47^{+8}_{-6} \times 10^{-4}\, [M_{\odot}] \qquad (4)$$

The binary mass function provides a lower limit to the mass of the unseen companion. The minimum mass of the companion can be approximately estimated as the maximum value between f and $f^{1/3}M_2^{2/3}$. Adopting a mass of $M_2[M_{\odot}] = 0.8$ for the seen star we obtain $M_1[M_{\odot}] > 0.14$ for the unseen companion.

The minimum orbital distance (or semi-major axis) of the star with respect to the centre of mass of the binary system can be computed as:

$$a_2 \sin i = [(P_{\mathrm{orb}} k_2)/(2\pi)](1 - e^2)^{1/2} = 1.571^{+0.153}_{-0.100}\, AU \qquad (5)$$

The dispersion of the ESPRESSO radial velocities after subtracting the best fit is now 47 m s^{-1} which is in line with the derived velocity jitter (Table 2). However, this is about 3 times larger than the mean error bar of the ESPRESSO radial velocity measurements, suggesting the presence of additional signal of relatively smaller amplitude. Pulsation, activity or the presence of a planetary motion are discussed in Aguado et al. (2022). The residuals of ESPRESSO RVs as shown in the inner panel within the centre panel of Fig. 2 after subtracting the orbital solution (black line) have been analysed for periodicity and did not show any obvious peak in the periodogram.

Table 2. Revised orbital parameters of HE 0107−5240 from the Markov Chain Monte Carlo (MCMC) analysis.

Parameter	MCMC Priors	Results
	Keplerian orbit	
k_2 [km s^{-1}]	$\mathcal{LU}$ (0.1, 5)	$1.67^{+0.08}_{-0.07}$
P_2 [d]	$\mathcal{LU}$ (1000, 75000)	10560^{+786}_{-518}
$T_2 - 2450000$ [d]	$\mathcal{U}$ (-4000, 3500)	494^{+492}_{-706}
ω [rad]	$\mathcal{U}$ (-π, π)	$-2.87^{+0.20}_{-0.16}$
e	$\mathcal{U}$ (0, 1)	$0.24^{+0.08}_{-0.08}$
	Other terms	
jitter$_{\mathrm{UVES}}$ [km s^{-1}]	$\mathcal{LU}$ (0.01, 5.0)	$0.24^{+0.08}_{-0.06}$
jitter$_{\mathrm{HRS}}$ [km s^{-1}]	$\mathcal{LU}$ (0.01, 5.0)	$0.03^{+0.08}_{-0.02}$
jitter$_{\mathrm{ESPRESSO}}$ [km s^{-1}]	$\mathcal{LU}$ (0.01, 5.0)	$0.03^{+0.01}_{-0.01}$
jitter$_{\mathrm{HARPS}}$ [km s^{-1}]	$\mathcal{LU}$ (0.01, 5.0)	$0.05^{+0.12}_{-0.03}$
$\gamma - 46.5$ [km s^{-1}]	$\mathcal{U}$ (-3.0, 3.0)	$0.35^{+0.14}_{-0.17}$

Note: the uncertainties of each quantity show the 16th and 84th percentile that covers the 68% ($1-\sigma$) of all samples.

5. Chemical Analysis

5.1. Stellar parameters

By using Gaia DR3 (Gaia Collaboration et al. 2023) photometry and parallax corrected by zero-point (−0.03783) as suggested by Lindegren et al. (2021), with reddening Av = 0.0344 from Schlafly & Finkbeiner (2011), we derive: T_{eff}= 5111 K and log g= 2.46 [cgs], as described in Caffau et al. (2024b). If the zero-point correction is not applied, the derived stellar parameters would be T_{eff}= 5116 K and log g= 2.20 [cgs]. Using the former value of the surface gravity (zero-point applied), the position of the star in a Gaia colour-magnitude diagram (CMD) agrees well with a BASTI isochrone (Pietrinferni et al. 2021a) for an age of 13 Gyr and [Fe/H] = −2.2 (see Fig. 3). The mass range implied by the two aforementioned surface gravities is 0.77–0.78 M$_{\odot}$. In the case the zero-point is not applied, the position of the star is still compatible with the [Fe/H] = −2.2 isochrone, but agrees better with the one of the same age and at [Fe/H] = −3.2. The position of HE 0107−5240, with the parameters corrected by the zero-point, in the Gaia CMD matches only marginally with a BASTI isochrone for an age of 13 Gyr and [Fe/H] = −3.2 (this is the lowest [Fe/H] value provided by BASTI isochrones). It is true that the metallicity of HE 0107−5240 is $\log Z/Z_{\odot} \approx -2.4$, due to its very high over-abundance of CNO with respect to Fe. The high carbon abundance leads to strong CH lines in the blue/UV spectral range, making the star to appear much redder in the $G_{\mathrm{BP}} - G_{\mathrm{RP}}$ colour compared to stars with a scaled Solar abundance pattern. This could be an explanation why a star with [Fe/H] = −5.56 (Aguado et al. 2022) is compatible with an isochrone 2-3 dex more metal-rich. But we have to bear in mind that to build the isochrones, whatever the position in the HR diagram, all the models are computed with the same mixing length value. This is especially problematic for evolved stars (see Manchon et al. 2024) and the fact is clear and discussed in the sample of giant stars investigated by Caffau et al. (2025).

Regarding the reddening, we note that the star has a very low extinction. This is confirmed by the absence of diffuse interstellar bands (DIBs) in the high-quality ESPRESSO spectrum. The interstellar Na I doublet lines are visible but weak and their equivalent widths confirm the low extinction. In fact the position in the sky of HE 0107−5240 (l = 296.5° and b = −64.49°) coincides with a well known window in the local interstellar matter

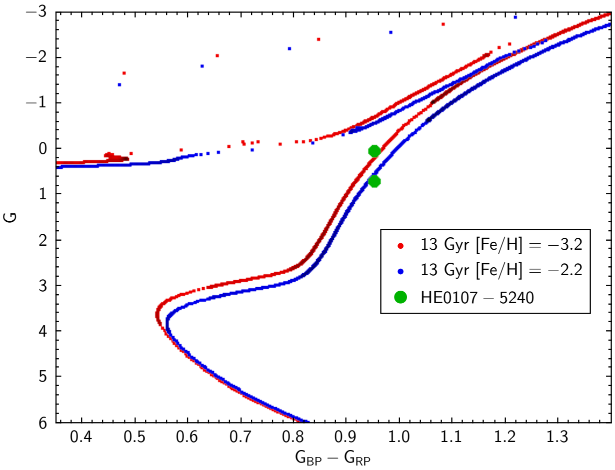

Fig. 3. BASTI isochrones (Pietrinferni et al. 2021b) in a Gaia colour-magnitude diagram. The two green points correspond to HE 0107−5240, assuming surface gravities of $\log g = 2.20$ (upper point) and 2.46 (lower point), respectively.

where the photons from the star intercept relatively small clouds in the Solar vicinity.

The stellar parameters used in the analyses of this star in the literature (see Table A.1) are: $T_{\rm eff}$= 5100 K and log g= 2.2 (Christlieb et al. 2002, 2004; Bessell et al. 2004; Yong et al. 2013; Aguado et al. 2022; Molaro et al. 2023); $T_{\rm eff}$= 5130 K and log g= 2.2 (Collet et al. 2006); $T_{\rm eff}$= 5050 K and log g= 2.3 (Ezzeddine et al. 2017); $T_{\rm eff}$= 5300 K and log g= 2.5 (Sitnova et al. 2019). We here adopted $T_{\rm eff}$= 5100 K, log g= 2.2 and a microturbulence of 2.2 $\rm km\,s^{-1}$, to be consistent with the previous works, especially Christlieb et al. (2004), Aguado et al. (2022) and Molaro et al. (2023). The two latter papers analysed a combined spectrum derived from the same ESPRESSO observations, but obtained with fewer exposures.

Using the Gaia parallax, the G magnitude and the bolometric correction derived from the grid of ATLAS 9 fluxes (Mucciarelli et al. in prep.), we estimated the luminosity of the star to be $\log(L/L_\odot) = 1.67 \pm 0.02$, where the error takes into account both the error on the parallax and on the magnitude G, but it is dominated by the error on the parallax. Although red giant stars are not in a very favourable position in the Hertzsprung-Russel diagram to determine their age, we attempted to do so using the code SPInS (Lebreton & Reese 2020; Reese & Lebreton 2020). We used a grid of BASTI α-enhanced evolutionary tracks (Pietrinferni et al. 2006). The input parameters were $\log(T_{\rm eff})$, $\log(L/L_\odot)$ and $\log(Z)$. This choice ensures that the parameters of HE 0107−5240 are well within the range covered by the grid. Had we chosen [Fe/H] as metallicity indicator the value for HE 0107−5240 would lie outside the grid. In the inference we assumed a uniform prior on age requiring that it is smaller than the age of the Universe, 13.8 Gyr (Planck Collaboration et al. 2020). The resulting age is 7.6 Gyr±3.2 Gyr.

5.2. Spectral energy distribution

The VOSA service[5] provides as the best fit parameters: $T_{\rm eff}$= 5500 K and log g= 1.5. They indicate a considerably warmer $T_{\rm eff}$ than our adopted one and a lower surface gravity (see Sec. 5.1). The spectral energy distribution of the star, when compared to the flux derived from the model, does not show any UV nor IR excess.

5.3. Abundances

HE 0107−5240 is ultra-poor in Fe, but its C content is about 16% solar, making this star a CEMP star. In Table A.1 the abundances derived in the literature are shown. As expected several upper-limits are present, but, due to the low metallicity of the star, many of them are too loose to be significant. In particular, the upper limits of the heavy elements do not allow to clarify if HE 0107−5240 matches the criterion for a CEMP-no star. Abundances or upper-limits derived from the new high-quality spectrum are provided in Table A.2 and a discussion element by element is given below. For the main 1D LTE analysis we computed spectral synthesis by using SYNTHE with an ATLAS 9 model atmosphere (Kurucz 2005). In addition, we computed dedicated 3D model atmospheres with the CO5BOLD code (Freytag et al. 2012, plus updates) to estimate 3D (LTE) corrections for selected spectral lines. Details about the models and spectrum synthesis codes are provided in the appendix (B).

Lithium. No lithium from the Li I doublet at 670.7 nm is visible. We applied the Cayrel's formula[6] multiplied by a factor three because we consider the uncertainty at 3σ (see Cayrel 1988, S/N=230) and we obtained A(Li) < -0.14 dex.

Beryllium. The two Be II resonance doublet lines lie at 313.0442 and 313.1067 nm, both outside the wavelength coverage of ESPRESSO. The reddest Be II feature (313.1067 nm) is not clearly detected in the UVES spectrum (see Fig. 4), while the other line (313.0442 nm) is heavily blended with CH molecular features. If present, the 313.1 nm line is buried in the noise, with S/N $\sim$ 35. We therefore derive an upper limit (or tentative detection) of A(Be) $\lessapprox -2.06$, corresponding to [Be/H] $\lessapprox -3.44$ and [Be/Fe] $\lessapprox +2.12$. However, we note that a hint of the line is present at the expected position. If confirmed in the future, this feature could potentially originate from primary spallation processes involving energetic CNO particles from the progenitor of HE 0107−5240 colliding with the ambient medium. Even an upper limit slightly above [Be/Fe] $< +2.0$ dex is significant (assuming the star has not depleted its beryllium) as it argues against the existence of a primordial Be plateau (see Figure 5) predicted by some inhomogeneous cosmological models, albeit at lower abundance levels (Malaney & Fowler 1989; Thomas et al. 1994; Jedamzik & Rehm 2001; Nakamura & Hashimoto 2017).

Carbon. The new spectrum does not alter the derived carbon abundance, as the CH G-band features are so strong that do not benefit from an increased S/N. To determine the carbon isotopic ratio, we selected regions in the observed spectrum where clean pairs of ^{12}CH and ^{13}CH lines are present. These lines arise from the same electronic transitions, but the ^{12}CH features are significantly stronger due to the stellar atmosphere containing approximately two orders of magnitude more ^{12}C than ^{13}C.

Our approach differs from that of Molaro et al. (2023) in that we used different spectral regions and simultaneously fit both the total carbon abundance and the isotopic ratio. Several wavelength intervals containing matched ^{12}CH and ^{13}CH lines were

[5] http://svo2.cab.inta-csic.es/theory/vosa

[6] $\sigma_{\rm EW} = 1.6 \times \sqrt{\rm PixelSize \times FWHM}/({\rm S/N})$

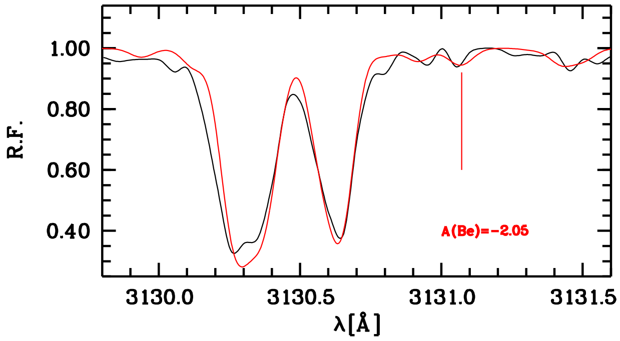

Fig. 4. Observed residual flux of the spectrum (solid black) in the wavelength range of the 313.1 nm Be II resonance doublet, compared to synthesis (solid red). The position of the Be II 313.1 nm line is marked with a vertical red line.

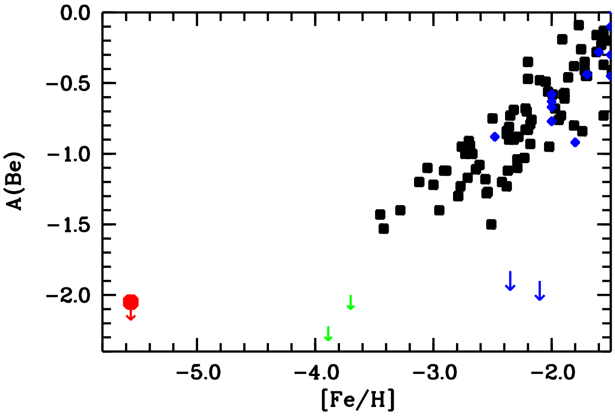

Fig. 5. Beryllium abundance in HE 0107−5240 (red symbol) compared to the Galactic behaviour Data from Boesgaard et al. (2011, black symbols) and Smiljanic et al. (2009, blue symbols) and the upper limits for 2MASS J18082002–5104378 and BD+44 493 (Spite et al. 2019, green symbols).

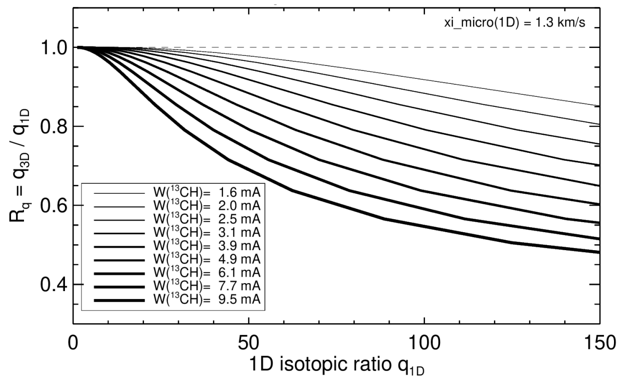

Fig. 6. 3D correction factor for the $^{12}C/^{13}C$ isotopic ratio versus the 1D isotopic ratio for different strengths of the ^{13}CH component of the 423.1 nm line pair. According to this diagram, a 1D isotopic ratio of 100 with a ^{13}CH equivalent width of 2 mÅ would translate to a 3D isotopic ratio of ≈ 90.

selected (5 ranges), and we performed a global fit using both parameters as free variables. This analysis yielded: (i) a carbon abundance of A(C) = 6.72 ± 0.02, where the uncertainty represents the region-to-region scatter (thus, a formal error), and (ii) an isotopic ratio of $^{12}C/^{13}C = 110 \pm 12$. Our carbon abundance is in excellent agreement with the value of A(C) = 6.75 reported by Molaro et al. (2023), and the isotopic ratio is consistent within 1.7σ with their result of $^{12}C/^{13}C = 87 \pm 6$.

To evaluate the impact of 3D effects, we computed the 3D (LTE) correction for the ^{12}CH line at 423.1 nm, obtaining a correction of −0.65 dex for the ^{12}C abundance. To assess the 3D correction of the isotopic ratio, we focused on the same spectral region, examining pairs of ^{12}CH and ^{13}CH lines sharing the same electronic transition. While both lines experience similar 3D effects at equal line strengths, in practice their strengths differ significantly. For a solar carbon isotopic ratio, the equivalent width (EW) of the ^{12}CH line is tens of times larger than that of the corresponding ^{13}CH line.

We computed the 3D correction factor of the $^{12}C/^{13}C$ isotopic ratio, R_q, as the ratio of the isotopic ratios derived in 3D and in 1D, $R_q = q_{3D}/q_{1D}$ and expressed this as a function of q_{1D} for different choices of the ^{13}CH line's equivalent width, EW_{13}, as shown in Fig. 6. The correction is also sensitive to the adopted microturbulence. We used a value of 1.3 $km s^{-1}$, selected to ensure a flat 3D abundance correction with the strength of the 516.9 nm Fe II line (see below).

Unfortunately, the derived 3D corrections depend on the chemical composition, in particular the C, N, O abundances, adopted for the construction of the 3D atmosphere and the 1D reference model. All 3D results reported above are based on a 3D (and 1D reference) model with a solar chemical composition scaled down by −4.0 dex, except for the α elements (including O but not C) that are enhanced by +0.4 dex relative to the other metals. Compared to the abundances derived for HE 0107–5240 in this work, C and O are too low by about −2.3 and −0.65 dex, respectively, in this model.

As an alternative, we also computed a pair of 3D – 1D models where the carbon and nitrogen abundances are enhanced by +3.0 dex and the oxygen abundance by +2.6 dex with respect to the previous case. Again, these C, N, O abundances are not representative of HE 0107–5240, now C and O are too high by about 0.7 and 2.0 dex, respectively. The C/O ratio is ∼ 0.5 instead of ∼ 10.

With the same procedure, we derived the 3D correction for the C abundance and the 3D correction for the $^{12}C/^{13}C$ isotopic ratio. As already found by Gallagher et al. (2017), the 3D correction is smaller (only about −0.2 dex) and the 3D correction factor for the C isotopic ratio increases from ∼ 0.8 to ∼ 1.1, implying that the 3D corrected isotopic ratio is larger than what is derived in 1D. What is important to underline here is that a robust result, beyond all uncertainties of the modelling, is that HE 0107–5240 has a high $^{12}C/^{13}C$ isotopic ratio ($\gtrsim 90$), ruling out any mixing with CNO processed material.

More reliable 3D corrections can only be obtained from a future 3D model based on custom-made opacity tables with consistent CNO abundances.

Nitrogen. The NH band at 336 nm is outside the wavelength coverage of ESPRESSO. We then used the UVES 346 spectrum to investigate it. We inspected this 336 nm NH band by using the molecular data provided by Fernando et al. (2018) and we derived A(N)=4.42 ([N/H] = −3.44 and [N/Fe] = +2.12). The 3D correction on the N abundance from this band is −0.58 dex, that, if applied, would decrease the [N/Fe] ratio to 1.6 dex.

Oxygen. No atomic or molecular useful line is available in the wavelength range of ESPRESSO. The OH lines in the UV range of a UVES spectrum have been already investigated by Bessell et al. (2004). We selected the OH lines in the list sug-

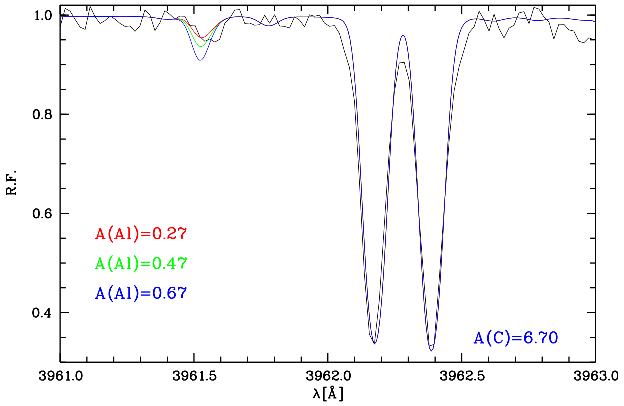

Fig. 7. Observed spectra (solid black) in the range of the Al I 396.1 nm line: tentative detection of Al (solid red) and other syntheses (solid blue) to show the Al line.

gested by Prakapavičius et al. (2017), as the molecular data we adopted are from their table A.1. We investigated ten OH lines and we derived ⟨A(O)⟩ = 5.72 ± 0.09. With a solar oxygen abundance of 8.76 (see Table A.2), we obtained [O/H] = −3.04 and [O/Fe] = +2.52 dex. The 3D effects on molecular lines are strong. The average corrections we derive is −0.58 ± 0.07 dex, but we have to stress that the corrections have been computed without taking into account scattering in the synthesis of both 1D and 3D profiles.

Sodium. The two Na I-D resonance lines are strong in the spectrum, providing an abundance of A(Na)=1.64. According to Andrievsky et al. (2007), NLTE corrections for the Na I D lines are small at extremely metal-poor regime. Two weak features due to Galactic interstellar absorption, account for the very low reddening.

Aluminium. At the wavelength of the strongest Al I line at 396.1 nm, a feature compatible with the Al line is visible. However, on the red side there is a spike due to noise that makes the detection uncertain. Either this is a tentative Al detection with an abundance of A(Al) = 0.27; or we have a conservative higher upper limit at A(Al) < 0.47. In both cases the star is poor in Al with [Al/Fe] = −0.64: or [Al/Fe] < −0.44 (see Fig. 7). The Al resonance lines are affected by strong NLTE effects. For the well known star CD–38:245, which has stellar parameters similar to HE 0107−5240, Andrievsky et al. (2008) derived a NLTE correction of +0.74 dex. The NLTE correction for Fe, according to the MPIA website[7] (hereafter MPIA), is about +0.55 dex (see below the paragraph on iron). So, taking into account the NLTE corrections for Al and Fe, the star is compatible to be solar in the [Al/Fe] ratio.

Silicon. The strong Si I line at 390.5 nm is not clearly visible in the spectrum, but there is a hint of a line that could be attributed to the Si I line. We provide a conservative upper limit of A(Si) < 1.8 corresponding to [Si/Fe] < −0.16. In fact, we guess a feature, compatible with the noise, at the expected wavelength, corresponding to a lower Si abundance (A(Si) ∼ 1.6, [Si/Fe] ∼ −0.36). For this line, the NLTE corrections provided in the web-site MPIA are large (+0.31 dex) when adopting a metallicity of −5.0 for the star, but still smaller than the NLTE correction of Fe. At metallicity −4.0 the NLTE correction for both elements are much smaller (+0.1 dex for Si and +0.3 dex for Fe).

Sulphur. The strongest S I feature available in the ESPRESSO spectrum is the strongest triplet of the Mult. 8 at 675.7 nm. However, this feature is already weak in solar-metallicity or slightly metal-poor stars and the upper-limit we derive (A(S) < 5.2) is not significant. The UVES spectra with setting 860 nm host the stronger S I lines of Mult. 1. We selected the S I lines at 922.8 and 923.7 nm, which are free from telluric absorption. The averaged spectrum from 4 OBs provided a much more stringent upper-limit at A(S) < 4.40 ([S/Fe] < 2.80) but still non-significant. The S I line of Mult, 1 are very sensitive to NLTE effects. According to Takeda et al. (2005), for the line at 923.7 nm a NLTE correction of about −0.5 dex is expected for a metallicity of −4.0.

Potassium. The strong K I line at 769.8 nm is not visible in the spectrum of HE 0107−5240 and no telluric contamination affect the position of the line. We took into account the S/N ratio of 200 and using Cayrel's formula we derived an upper-limit of [K/Fe] < 1.50, which is not significant. Looking at the computations from Andrievsky et al. (2010), the NLTE correction for this line is not large, of the order of +0.1 dex.

Scandium. Two Sc II lines (361.38 and 363.07 nm) are available in the UVES 346 spectrum. In spite of the low S/N ratio in this spectral region we have been able to detect the 361.3 nm Sc II line and we derived A(Sc) = −2.3 ([Sc/H] = −5.40).

Chromium. Due to the good spectral quality (S/N of almost 100), at 425.43 nm a feature is visible in the spectrum. According to the synthesis this is a blend of the Cr I line at 425.43 nm with two CH lines, so the contribution is due to CH. In the green wavelength range, at 520 nm, the S/N is almost 200 and three Cr I lines are not visible. By using Cayrel's formula, we derived an upper-limit too small, that we think too optimistic for such weak lines. We think that an upper-limit of A(Cr) < 0.30 and [Cr/Fe] < 0.22 is reasonable. The Cr upper-limit is not significant to draw conclusions on the star. On top of that, the NLTE correction is large and positive (of +0.8 dex in the case of metallicity −4.0) according to MPIA. This value is larger than the NLTE correction for Fe, fact that makes this upper-limit non significant.

Manganese. The Mn I at 403.3 nm is not visible, providing (using Cayrel's formula) a stringent upper-limit (A(Mn) < −0.50. But the NLTE correction expected from these line is large (∼ 1 dex, see Bergemann & Gehren 2008).

Iron. We keep A(Fe) from neutral lines from Aguado et al. (2022, A(Fe)=1.96) because the value we derived from the latest ESPRESSO combined spectrum is just 0.005 dex higher. Christlieb et al. (2004) provided upper limits on A(Fe) from two Fe II lines at 501.8440 and 516.9028 nm (Nave & Johansson 2013). Of the two lines the 516.9 nm line is weak but clearly visible in the ESPRESSO spectrum. We adopted log gf = −1.0 from Meléndez & Barbuy (2009), while Schnabel et al. (2004) provide a log gf of −0.87. We derived A(Fe)=1.74 from line-profile fitting (see Fig. 8). From the other two Fe II lines ex-

[7] https://nlte.mpia.de/gui-siuAC_secE.php

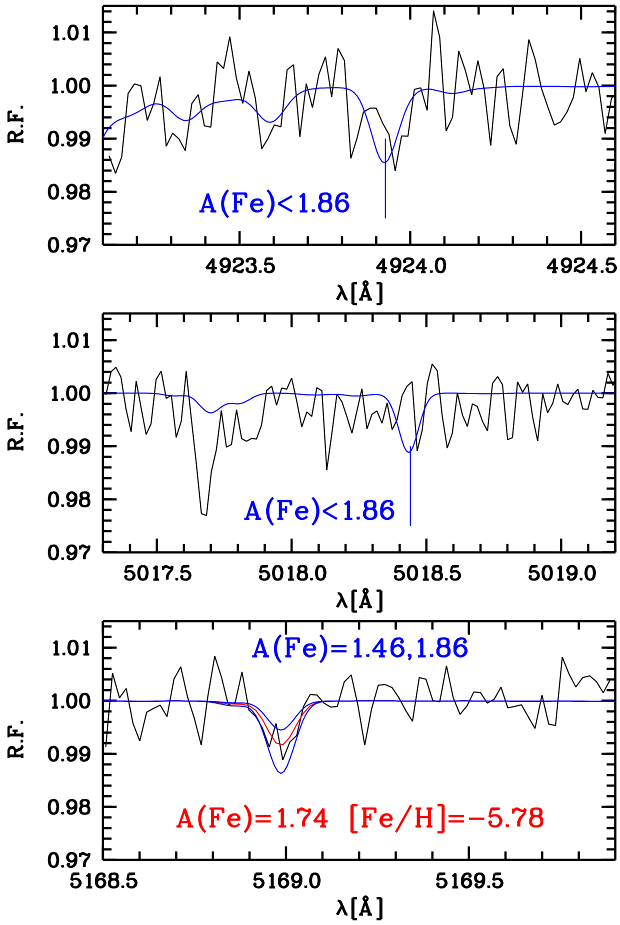

Fig. 8. Observed spectra (solid black, from top to bottom Fe II 492.3, 501.8 and 516.9 nm), compared to the best fit (solid red) and synthetic profile to provide uncertainty and upper-limit (solid blue).

pected to be strong enough to be visible in extremely metal-poor stars (492.3921 and 501.8440 nm), we derived just an upper-limit, consistent with the abundance from the 516.9 nm line (see Fig. 8). As expected, according to MPIA, the NLTE correction for the 516.9 nm line is very small (0.03 dex). Our 3D LTE model provides a 3D correction for this line of about +0.1 dex. In the UVES setting 346, we detected also the Fe II line at 322.774 nm for which we derived A(Fe)=1.67 (with a log gf of −1.014), in good agreement with the Fe II line in the ESPRESSO spectrum.

Selecting among the Fe I lines investigated by Aguado et al. (2022), 12 are present in the database MPIA to derive 1D NLTE correction for iron. From these lines, we derived a NLTE correction of +0.54, adopting a model with parameters: $T_{\rm eff}$=5100 K, log g=2.2, [Fe/H] = −5.0 and microturbulence of 2.2 $\rm km s^{-1}$ (−5.0 is the lowest metallicity provided). By applying the NLTE correction to the A(Fe)=1.96 derived from Fe I lines, we have a disagreement with the abundance from the A(Fe)=1.74 Fe II line. The NLTE correction from the same Fe I line adopting a metallicity −3.0, compatible with the oxygen abundance, is +0.12 dex, and with a metallicity −2.0, compatible with the C content, is +0.08 dex. Clearly, a 'high' NLTE correction in A(Fe) from neutral lines brings tension with the Fe abundance derived from the ionised lines.

Cobalt. The Co I UV lines (345.35 and 352.98 nm) are outside the wavelength range of ESPRESSO, but they are in the UV UVES range. The result from the UVES spectrum is not so clear.

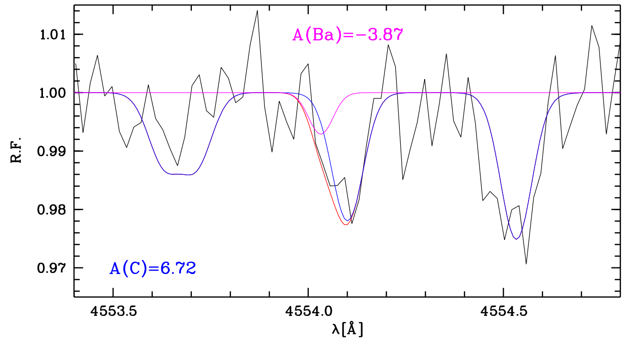

Fig. 9. Observed spectra (solid black) in the range of the Ba II 455.4 nm line compared to synthesis of the upper-limit on Ba (solid pink), synthesis on the contribution of CH (sold blue) and synthesis with CH and Ba upper-limit (solid red).

(i) The feature at 345.35 nm is compatible with A(Co) ∼ −0.30. The line is blended with a non-reproduced NH line, but the blend is not affecting the abundance derived. (ii) The two Co I lines at 352.9 nm are consistent and provide A(Co) ∼ 0.30 and [Co/H] = −4.62.

Zinc. The line at 481.5 nm is the strongest Zn I line available in the wavelength range provided by ESPRESSO. We did not detect the line in the spectrum because it is too weak. Any upper-limit is not stringent and Cayrel's formula was too optimistic, so we over-plotted synthetic spectra and we derived an upper-limit on Zn for A(Zn) < 1.02 which is lower than the previous values provided in the literature (see Table A.1) but sill not significant. Looking in the tables by Takeda et al. (2005), the NLTE correction is positive but not large (∼ 0.1 dex).

Strontium. The 407.7 nm Sr II line is not detectable in the spectrum. We computed the S/N ratio as 90 and, using Cayrel's formula (multiplied by three, Cayrel 1988), we derive A(Sr) < −3.89 ([Sr/Fe] < −1.25), which is a very stringent upper-limit. Looking at a star (CD–38:245) with similar parameters investigated by François et al. (2007), Andrievsky et al. (2011) provide a NLTE correction of +0.23 dex. Also taking into account the NLTE correction, the star is Sr-poor, moreover considering the NLTE correction for Fe from neutral lines provided in the literature (and in contradiction with our results on Fe II) is positive and expected to be larger.

Barium. Deriving a Ba detection or a stringent upper-limit is extremely important in the case of CEMP stars to understand to which group they belong. A low Ba abundance or upper-limit providing [Ba/Fe] < 0 would imply that the star is a CEMP-no. The Ba II line at 455.4 nm is blended in this C-rich star with CH molecules, that have to be taken into account. The CH line shows an asymmetry that could be due to the Ba contribution. The S/N ratio per pixel in the wavelength range is 160, that, by using Cayrel's formula, provides at 3σ A(Ba) < −3.87 ([Ba/H] = −6.04 and [Ba/Fe] = −0.48 when using A(Fe) from Fe I lines). The asymmetry in the CH line is more than justified by this upper-limit. In Fig. 9 we provide the observed spectrum compared to the synthesis with the CH contribution, with the upper-limit on Ba and with both. Considering the 1D-NLTE correction for CD–38:245 (François et al. 2007), Andrievsky et al. (2011) provide +0.32 dex, but the NLTE of A(Fe) from Fe I lines is expected to be larger.

Europium. The Eu II line at 412.973 nm is not visible in the spectrum. In the wavelength range we measured a S/N around 80 that, by using Cayrel's formula at 3σ, implies an upper-limit of A(Eu) < −3.0 but few spike of noise pushed us to adopt A(Eu) < −2.67. Both values are not significant.

6. Discussion

HE 0107−5240 is a Halo binary system with a prograde Galactic orbit. Its abundances reflect the chemical composition of the cloud from where the system was formed. The star belong to a binary system with an estimated period of about 29 y.

6.1. Stellar chemistry

6.1.1. The carbon isotopic signature: high ^{13}C abundance

Notably, the absolute abundance of ^{13}C in HE 0107−5240, A(^{13}C) = 4.68, exceeds that of nitrogen (A(N) = 4.42) and is second only to oxygen (A(O) = 5.72) and ^{12}C (A(^{12}C) = 6.72), underscoring the significant presence of ^{13}C in the stellar atmosphere.

The carbon isotopic ratio (^{12}C/^{13}C) measured in HE 0107−5240 (also accounting for 3D corrections) is consistent with the value reported by Molaro et al. (2023) and slightly higher than those observed in the sample of unmixed giant stars analysed by Spite et al. (2006).

Nonetheless, the derived ratio remains well below the predictions of the zero-metallicity stellar models, which typically yield ^{12}C/^{13}C ratios exceeding 1000 (e.g. Roberti et al. 2024). Ratios in the range ^{12}C/^{13}C = 50–100 can be produced when the hydrogen- and helium-burning shells merge during the pre-supernova evolution of massive stars. This scenario is exemplified by the 25$M_\odot$ zero-metallicity model with an initial rotational velocity of 300 km s^{-1} presented by Roberti et al. (2024). Incorporating the nucleosynthetic yields from such models into a Galactic chemical evolution framework, Rizzuti et al. (2025) successfully reproduced observed abundance patterns (provided that H-He shell merging also occurs in stars with metallicities up to [Fe/H] = −3.0). The carbon isotopic ratio observed in HE 0107−5240 also rules out self-pollution from an AGB companion as the origin of its carbon enhancement, as such a process would produce ratios of ^{12}C/^{13}C < 10. Instead, the value is consistent with those found in other unevolved carbon-enhanced metal-poor stars, such as HE 1327−2326 and HE 0233−0343 (see Molaro et al. 2023). It is important to note, however, that measuring isotopic ratios above ∼ 100 in metal-poor stars is observationally challenging, if not unfeasible. Therefore, published lower limits below this threshold may still be compatible with much higher intrinsic values, potentially exceeding 1000.

6.1.2. Reevaluating NLTE effects: iron lines show LTE consistency

The LTE iron abundances derived from both neutral and ionised lines in HE 0107−5240 are in perfect agreement within the uncertainties (as already noted by Christlieb 2008), without applying any corrections, contrary to what NLTE studies typically predict. The Fe II line at 516.9 nm forms at approximately $\log\tau \sim -1$, relatively deep within the stellar atmosphere. Since Fe II is the dominant ionisation state of iron under these conditions, this line is expected to form close to LTE. The agreement between Fe I and Fe II abundances thus implies that NLTE effects on Fe I must be small for HE 0107−5240.

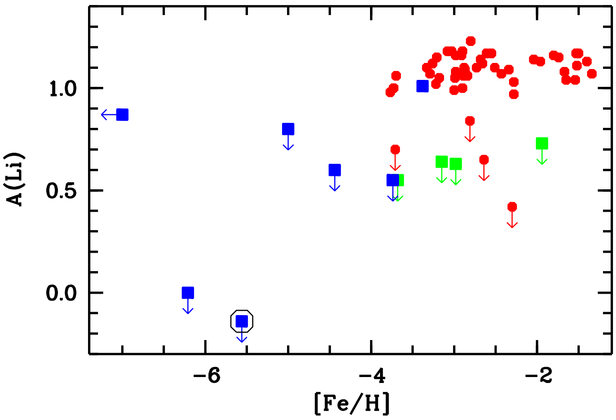

Fig. 10. Update figure of Figure 2 from Mucciarelli et al. (2022), with same symbols: red filled circles normal star, blue and green filled squares CEMP stars with 'low' and 'high' A(C), respectively. HE 0107−5240 is highlighted by a black circle.

This finding stands in contrast with the literature, where significant positive NLTE corrections are generally reported for neutral iron lines in extremely metal-poor stars (see, e.g., Amarsi et al. 2016; Ezzeddine et al. 2017). For example, Nordlander et al. (2017) investigated 3D-NLTE effects on iron in the ultra iron-poor star SMSS 0313–6708, which has stellar parameters nearly identical to those of HE 0107−5240; in fact, their model was computed specifically for HE 0107−5240. They found a 3D-NLTE correction of approximately +0.8 dex.

If we were to force the Fe II abundance to match the lower Fe I abundance derived by Ezzeddine et al. (2017) under NLTE assumption, we would need to increase the surface gravity of HE 0107−5240 by more than 2 dex, effectively classifying it as a Turn-Off star. However, this scenario is clearly inconsistent with the Gaia parallax and with the observed profiles of Hα and other Balmer lines, whose wings are too narrow to support such high gravity.

This unexpected result for HE 0107−5240, which is supported by a preliminary consistent result for SMSS J160540.18–144323.1 (Nordlander et al. 2019) discussed in the Appendix C, challenges current expectations and highlights the need for further investigation into 1D- and 3D-NLTE effects in the most iron-poor stars.

6.1.3. Lithium depletion

According to its stellar parameters, HE 0107−5240 should lie on the Mucciarelli plateau (Mucciarelli et al. 2022), which implies an expected lithium abundance of A(Li) ∼ 1.09. In Fig. 10 we reproduce Figure 2 from Mucciarelli et al. (2022), adding SMSS J1505–1443 (Nordlander et al. 2019) and SDSS J1313–0019 (Allende Prieto et al. 2015) and updating value for HE 0107−5240. The upper limit on lithium (A(Li) < −0.14) of HE 0107−5240 is consistent with an absence of lithium, suggesting that either the star has destroyed its lithium or it formed from a gas cloud already devoid of lithium.

It is true that several CEMP-no stars fall below the Mucciarelli plateau (see Figure 2 in Mucciarelli et al. 2022), yet some do lie on the plateau. For example, Matsuno et al. (2017) measured lithium at the Spite plateau level in two CEMP-no dwarf stars with metallicities around [Fe/H] ∼ −3.0. This indicates that the nature of their progenitors alone cannot explain the higher incidence of lithium depletion at low metallicities. As discussed in Molaro et al. (2023), the mechanism responsible for lithium

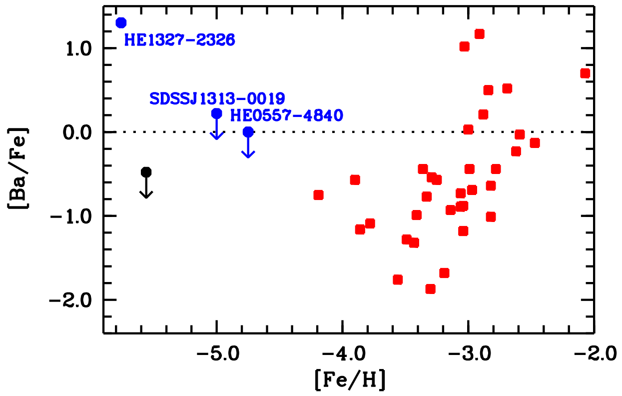

Fig. 11. [Ba/Fe] versus [Fe/H] (black arrow) compared to the sample in François et al. (2007) (red full red). Three CEMP stars HE 1327–2326 (Molaro et al. 2023) SDSSJ 131326.89–001941.4 (Frebel et al. 2015, ApJ 810,27) and HE 0557–4840 (Norris et al. 2007, ApJ 670, 774) are added as blue symbols.

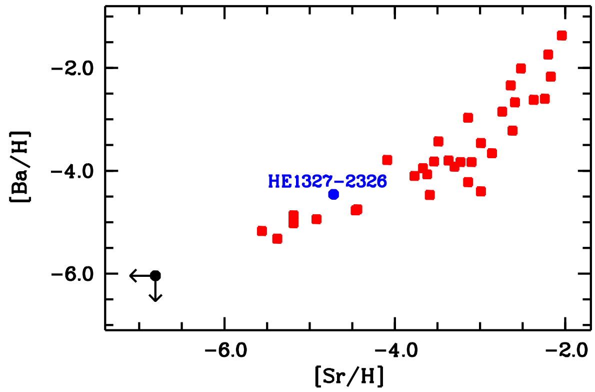

Fig. 12. [Ba/H] versus [Sr/H] (double black arrow) compared to the sample in François et al. (2007) (red full red) and to HE 1327–2326 (Molaro et al. 2023, blue filled circle).

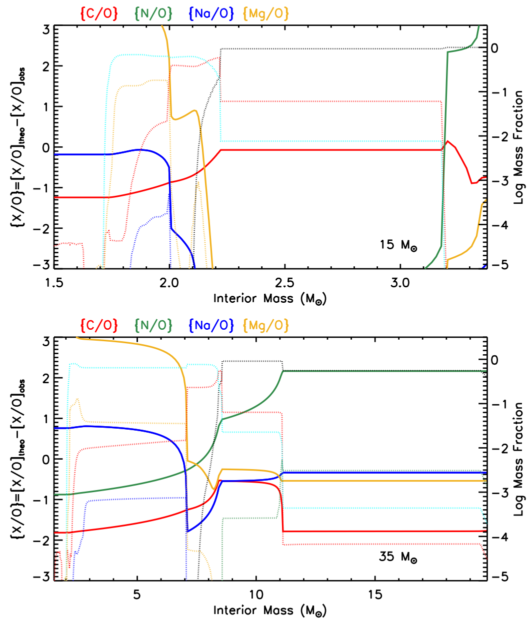

Fig. 13. Abundance ratios C, N, Na, Mg/O as a function of remnant mass for a zero-metallicity 15 $M_\odot$ (top) and 35 $M_\odot$ (bottom) star (Limongi & Chieffi 2012) after the explosion (solid thick lines, left y-axis). The abundance ratio X/O is defined as the difference between the predicted and observed [X/O] values. The right y-axis shows post-explosion interior profiles of ^{4}He (black dotted line), ^{12}C (red), ^{16}O (cyan), ^{23}Na (blue), and ^{24}Mg (orange).

depletion appears to correlate more strongly with extremely low iron abundance, rather than with destruction during the evolution of faint supernovae, the likely progenitors of CEMP-no stars.

An alternative explanation is that HE 0107−5240 is an evolved blue straggler, formed through the merger of two lower-mass stars, during which lithium could have been destroyed. Interestingly, the relatively young age we derived for HE 0107−5240 — unusual for a halo star — may support this hypothesis. However, given the large uncertainty in the age estimate, it remains consistent within 1.8σ with an age equal to that of the Universe.

6.1.4. n-capture elements

The new upper limit for barium in HE 0107−5240 satisfies the criterion for classification as a CEMP-no star. In Fig. 11, the star is compared to a sample of EMP stars (excluding CEMP stars) analysed under LTE assumption by François et al. (2007), and it displays a comparable [Ba/Fe] ratio. However, a striking contrast is seen with HE 1327−2326, which shows a high barium abundance of [Ba/Fe] = +1.0 (Molaro et al. 2023), highlighting the large diversity in the behaviour of neutron-capture elements at low metallicities. Also in the [Ba/H] vs. [Sr/H] plane, HE 0107−5240 is consistent with metal-poor stars (see Fig. 12).

Hansen et al. (2015) proposed the existence of a floor in the absolute barium abundance at A(Ba) ∼ −2.0 for CEMP-no stars. However, HE 0107−5240, with its extremely low [Fe/H] and an upper limit of A(Ba) < −3.87, lies well below this proposed floor and below all upper limits reported in their study (see their Figure 13). This suggests that either the barium floor occurs at a lower level than previously thought, or it may not exist at all.

6.2. Origin of HE 0107−5240

Limongi et al. (2003) proposed a model to explain the observed abundance ratios in HE 0107−5240 by invoking the ejecta of primordial core-collapse supernovae. Specifically, they suggested that elements heavier than Mg were synthesised in one or more 'normal' Population III core-collapse supernovae, while the lighter elements originated from enrichment by a failed Pop III supernova - i.e., one that left behind a very massive remnant. This scenario was based on a detailed analysis of pre-supernova models and explosive yields published by Chieffi & Limongi (2002) and Limongi & Chieffi (2002).

In particular, they found that stars with initial masses around 35 $M_\odot$ underwent partial mixing between the He convective shell and the tail of the H shell. This mixing, which is relatively common in zero-metallicity massive stars (see, e.g., Fujimoto et al. 1990; Chieffi et al. 2001; Limongi & Chieffi 2012; Roberti et al. 2024), leads to the synthesis of C, N, Na, and Mg in relative proportions consistent with those observed in HE 0107−5240.

A quantitative analysis using these models demonstrated that the observed abundance pattern (specifically, the elements C, N, Na, Mg, Ca, Ti, and Ni) could be reproduced by combining the yields of a 15$M_\odot$ 'normal' Pop III supernova with those of a 35$M_\odot$ model in which the mass cut was located within the He shell, corresponding to a remnant mass of 9.4 $M_\odot$ (see Figure 3 in Limongi et al. 2003).

Subsequent spectroscopic studies of HE 0107−5240 allowed for a determination of the [O/Fe] abundance ratio (see Table A.1 for literature values and Table A.2 for our determination), which was unavailable at the time of the original analysis. The measured oxygen abundance — particularly the observed ratio [C/O] > 1, implying a super-solar C/O ratio — presents a potential challenge for the model. This is because the only region in a massive star where ^{12}C exceeds ^{16}O in abundance is the He convective shell. In this zone, He burning is incomplete, leading to a significant accumulation of ^{12}C before it is fully converted into ^{16}O.

As shown in the upper panel of Fig. 13, a recent 15M$_{\odot}$ zero-metallicity model (Limongi & Chieffi 2012) exhibits a [C/O] ratio within the He convective shell (between mass coordinates ∼ 2.2 and ∼ 3.2$M_{\odot}$) that matches the observed value. Thus, placing the mass cut within this region yields ejecta with a [C/O] ratio in excellent agreement with observations. However, due to the initial zero metallicity, this region does not produce ^{14}N, which is observed in HE 0107−5240. Therefore, although such a mass cut can reproduce the observed [C/O], it fails to account for the observed [N/O].

As previously discussed, significant ^{14}N and ^{13}C production in zero-metallicity stars requires partial mixing between the He convective shell and the overlying H-rich shell. Proton ingestion into the He shell triggers a primary CNO cycle, generating ^{14}N and ^{13}C from freshly synthesised ^{12}C. While this mixing process is relatively common in zero-metallicity stars, it occurs only in a limited mass range — typically between ∼ 25 and ∼ 35 $M_{\odot}$. Proton ingestion also alters the abundances of ^{12}C and ^{16}O, reducing the [C/O] ratio below the observed value in HE 0107−5240.

The bottom of Figure 13 shows the internal presupernova composition of a 35M$_{\odot}$ model (Limongi & Chieffi 2012) where such partial He/H mixing occurred. In the mixed region of the He shell (mass coordinates ∼ 11 to ∼ 20$M_{\odot}$), the [C/O] ratio drops significantly, while [N/O] rises above the observed value. Conversely, in the deeper portion of the He shell (between ∼ 8.5 and ∼ 11 $M_{\odot}$) that remained unmixed, ^{12}C dominates over ^{16}O, resulting in a high [C/O] and low [N/O], along with [Na/O] and [Mg/O] values slightly below the observed ratios. These abundance patterns depend on the extent of He burning in the inner shell and the efficiency and depth of mixing with the H-rich envelope.

Among the models published by Limongi & Chieffi (2012), this peculiar internal structure is found only in the 35 M$_{\odot}$ case. However, due to the limited mass resolution of the available grid, it is currently not possible to fully explore how this behaviour varies with initial stellar mass. It remains plausible that models with intermediate or different initial masses could yield C, N, O, Na, and Mg abundance ratios more closely aligned with the observations. To investigate this possibility, we plan to conduct a more extensive and finely sampled study in future work.

7. Conclusions

The main conclusions are:

- Observations of HE 0107−5240 over a longer temporal baseline have refined the orbital period to 10560^{+786}_{-518} d (∼ 28.9 y), which is smaller than previously derived (Aguado et al. 2022).
- The binary system follows a halo prograde orbit around the Galactic centre.
- New stringent upper limits on Sr and Ba abundances confirm that HE 0107−5240 satisfies the CEMP-no classification. These limits do not support the existence of a floor in the absolute barium abundance at A(Ba) ∼ −2.0 for CEMP-no stars, as proposed by Hansen et al. (2015).
- Lithium remains undetected at levels much lower than those reported by Mucciarelli et al. (2022) for giants, implying that Li has been depleted either in the star itself or in its progenitor.
- The Fe abundances derived under LTE assumptions from both Fe I and Fe II lines are in good agreement, raising concerns about the reliability of published NLTE corrections for Fe I.
- The ^{12}C/^{13}C isotopic ratio is measured to be 110 ± 12, which is close to the solar value. We have shown that this ratio is sensitive to 3D NLTE effects, which tend to lower the derived value. The NLTE-corrected ratio is 87, higher than the average value observed in unmixed stars by Spite et al. (2006), yet still low enough for ^{13}C to be the third most abundant element in the star's atmosphere.

Acknowledgements. PB acknowledges support from the ERC advanced grant N. 835087 – SPIAKID. LM gratefully acknowledges support from ANID-FONDECYT Regular Project n. 1251809. This work has made use of data from the European Space Agency (ESA) mission *Gaia* (`https://www.cosmos.esa.int/gaia`), processed by the *Gaia* Data Processing and Analysis Consortium (DPAC, `https://www.cosmos.esa.int/web/gaia/dpac/consortium`). Funding for the DPAC has been provided by national institutions, in particular the institutions participating in the *Gaia* Multilateral Agreement. JIGH, DSA, RR and CAP acknowledge financial support from the Spanish Ministry of Science, Innovation and Universities (MICIU) projects PID2020-117493GB-I00 and PID2023-149982NB-I00. This research has made use of the SIMBAD database, operated at CDS, Strasbourg, France. PM warmly acknowledge Richard Hoppe for stressing the importance of the 3D/NLTE effects on the carbon isotopic ratio. NCS acknowledges funding by the European Union (ERC, FIERCE, 101052347). Views and opinions expressed are however those of the author(s) only and do not necessarily reflect those of the European Union or the European Research Council. Neither the European Union nor the granting authority can be held responsible for them. NJN was supported by FCT - Fundação para a Ciência e a Tecnologia through national funds by grants UIDB/04434/2020 and UIDP/04434/2020. The work of CJAPM was financed by Portuguese funds through FCT (Fundação para a Ciência e a Tecnologia) in the framework of the project 2022.04048.PTDC (Phi in the Sky, DOI 10.54499/2022.04048.PTDC). CJM also acknowledges FCT and POCH/FSE (EC) support through Investigador FCT Contract 2021.01214.CEECIND/CP1658/CT0001 (DOI 10.54499/2021.01214.CEECIND/CP1658/CT0001). MTM acknowledges the support of the Australian Research Council through Future Fellowship grant FT180100194 and through the Australian Research Council Centre of Excellence in Optical Microcombs for Breakthrough Science (project number CE230100006) funded by the Australian Government.

References

Aguado, D. S., Molaro, P., Caffau, E., et al. 2022, A&A, 668, A86
Allende Prieto, C., Fernández-Alvar, E., Aguado, D. S., et al. 2015, A&A, 579, A98
Amarsi, A. M., Lind, K., Asplund, M., Barklem, P. S., & Collet, R. 2016, MNRAS, 463, 1518
Andrievsky, S. M., Spite, F., Korotin, S. A., et al. 2011, A&A, 530, A105
Andrievsky, S. M., Spite, M., Korotin, S. A., et al. 2010, A&A, 509, A88
Andrievsky, S. M., Spite, M., Korotin, S. A., et al. 2007, A&A, 464, 1081
Andrievsky, S. M., Spite, M., Korotin, S. A., et al. 2008, A&A, 481, 481
Arentsen, A., Starkenburg, E., Shetrone, M. D., et al. 2019, A&A, 621, A108
Beers, T. C. & Christlieb, N. 2005, ARA&A, 43, 531
Beers, T. C., Preston, G. W., & Shectman, S. A. 1992, AJ, 103, 1987
Bensby, T., Feltzing, S., & Oey, M. S. 2014, A&A, 562, A71
Bergemann, M. & Gehren, T. 2008, A&A, 492, 823
Bessell, M. S., Christlieb, N., & Gustafsson, B. 2004, ApJ, 612, L61
Boesgaard, A. M., Rich, J. A., Levesque, E. M., & Bowler, B. P. 2011, ApJ, 743, 140
Bonifacio, P., Caffau, E., Ludwig, H. G., et al. 2018, A&A, 611, A68
Bonifacio, P., Caffau, E., Spite, M., et al. 2015, A&A, 579, A28
Bonifacio, P., Molaro, P., Adibekyan, V., et al. 2020, A&A, 633, A129
Bonifacio, P., Molaro, P., Beers, T. C., & Vladilo, G. 1998, A&A, 332, 672
Bonifacio, P., Monaco, L., Salvadori, S., et al. 2021, A&A, 651, A79
Bovy, J. 2015, ApJS, 216, 29

Bovy, J., Allende Prieto, C., Beers, T. C., et al. 2012, ApJ, 759, 131
Caffau, E., Bonifacio, P., François, P., et al. 2011a, Nature, 477, 67
Caffau, E., Bonifacio, P., Monaco, L., et al. 2024a, A&A, 684, L4
Caffau, E., Bonifacio, P., Monaco, L., et al. 2024b, A&A, 691, A245
Caffau, E., Katz, D., Bonifacio, P., et al. 2025, Astronomische Nachrichten, 346, e70025
Caffau, E., Ludwig, H. G., Steffen, M., Freytag, B., & Bonifacio, P. 2011b, Sol. Phys., 268, 255
Cayrel, R. 1988, in The Impact of Very High S/N Spectroscopy on Stellar Physics, ed. G. Cayrel de Strobel & M. Spite, Vol. 132, 345
Cayrel, R., Depagne, E., Spite, M., et al. 2004, A&A, 416, 1117
Chamberlain, J. W. & Aller, L. H. 1951, ApJ, 114, 52
Chieffi, A., Domínguez, I., Limongi, M., & Straniero, O. 2001, ApJ, 554, 1159
Chieffi, A. & Limongi, M. 2002, ApJ, 577, 281
Christlieb, N. 2008, Physica Scripta Volume T, 133, 014034
Christlieb, N., Bessell, M. S., Beers, T. C., et al. 2002, Nature, 419, 904
Christlieb, N., Gustafsson, B., Korn, A. J., et al. 2004, ApJ, 603, 708
Collet, R., Asplund, M., & Trampedach, R. 2006, ApJ, 644, L121
Collet, R., Hayek, W., Asplund, M., et al. 2011, A&A, 528, A32
Ezzeddine, R., Frebel, A., & Plez, B. 2017, ApJ, 847, 142
Fernando, A. M., Bernath, P. F., Hodges, J. N., & Masseron, T. 2018, J. Quant. Spectr. Rad. Transf., 217, 29
Feuillet, D. K., Sahlholdt, C. L., Feltzing, S., & Casagrande, L. 2021, MNRAS, 508, 1489
Foreman-Mackey, D., Agol, E., Ambikasaran, S., & Angus, R. 2017, AJ, 154, 220
François, P., Depagne, E., Hill, V., et al. 2007, A&A, 476, 935
Freytag, B., Steffen, M., Ludwig, H. G., et al. 2012, Journal of Computational Physics, 231, 919
Fujimoto, M. Y., Iben, Jr., I., & Hollowell, D. 1990, ApJ, 349, 580
Fulton, B. J., Petigura, E. A., Blunt, S., & Sinukoff, E. 2018, PASP, 130, 044504
Gaia Collaboration, Vallenari, A., Brown, A. G. A., et al. 2023, A&A, 674, A1
Gallagher, A. J., Caffau, E., Bonifacio, P., et al. 2017, A&A, 598, L10
Hansen, T., Hansen, C. J., Christlieb, N., et al. 2015, ApJ, 807, 173
Jedamzik, K. & Rehm, J. B. 2001, Phys. Rev. D, 64, 023510
Kurucz, R. L. 2005, Memorie della Societa Astronomica Italiana Supplementi, 8, 14
Kučinskas, A., Klevas, J., Ludwig, H. G., et al. 2018, A&A, 613, A24
Lardo, C., Mashonkina, L., Jablonka, P., et al. 2021, MNRAS, 508, 3068
Lebreton, Y. & Reese, D. R. 2020, A&A, 642, A88
Limberg, G., Placco, V. M., Ji, A. P., et al. 2025, ApJ, 989, L18
Limongi, M. & Chieffi, A. 2002, PASA, 19, 246
Limongi, M. & Chieffi, A. 2012, ApJS, 199, 38
Limongi, M., Chieffi, A., & Bonifacio, P. 2003, ApJ, 594, L123
Lindegren, L., Bastian, U., Biermann, M., et al. 2021, A&A, 649, A4
Lodders, K., Palme, H., & Gail, H. P. 2009, Landolt Börnstein, 4B, 712
Ludwig, H.-G. & Steffen, M. 2012, in Astrophysics and Space Science Proceedings, Vol. 26, Red Giants as Probes of the Structure and Evolution of the Milky Way, ed. A. Miglio, J. Montalbán, & A. Noels, 125
Ludwig, H. G. & Steffen, M. 2013, Memorie della Societa Astronomica Italiana Supplementi, 24, 53
Malaney, R. A. & Fowler, W. A. 1989, ApJ, 345, L5
Manchon, L., Deal, M., Goupil, M. J., et al. 2024, A&A, 687, A146
Matsuno, T., Aoki, W., Beers, T. C., Lee, Y. S., & Honda, S. 2017, AJ, 154, 52
Meléndez, J. & Barbuy, B. 2009, A&A, 497, 611
Molaro, P., Aguado, D. S., Caffau, E., et al. 2023, A&A, 679, A72
Mucciarelli, A., Monaco, L., Bonifacio, P., et al. 2022, A&A, 661, A153
Nakamura, R. & Hashimoto, M.-a. 2017, in 14th International Symposium on Nuclei in the Cosmos (NIC2016), ed. S. Kubono, T. Kajino, S. Nishimura, T. Isobe, S. Nagataki, T. Shima, & Y. Takeda, 020108
Nave, G. & Johansson, S. 2013, ApJS, 204, 1
Nordlander, T., Amarsi, A. M., Lind, K., et al. 2017, A&A, 597, A6
Nordlander, T., Bessell, M. S., Da Costa, G. S., et al. 2019, MNRAS, 488, L109
Norris, J. E., Ryan, S. G., & Beers, T. C. 1997, ApJ, 489, L169
Pietrinferni, A., Cassisi, S., Salaris, M., & Castelli, F. 2006, ApJ, 642, 797
Pietrinferni, A., Hidalgo, S., Cassisi, S., et al. 2021a, ApJ, 908, 102
Pietrinferni, A., Hidalgo, S., Cassisi, S., et al. 2021b, ApJ, 908, 102
Planck Collaboration, Aghanim, N., Akrami, Y., et al. 2020, A&A, 641, A6
Prakapavičius, D., Kučinskas, A., Dobrovolskas, V., et al. 2017, A&A, 599, A128
Reese, D. R. & Lebreton, Y. 2020, SPInS: Stellar Parameters INferred Systematically, Astrophysics Source Code Library, record ascl:2009.006
Rizzuti, F., Cescutti, G., Molaro, P., et al. 2025, A&A, 698, A118
Roberti, L., Limongi, M., & Chieffi, A. 2024, ApJS, 270, 28
Schlafly, E. F. & Finkbeiner, D. P. 2011, ApJ, 737, 103
Schnabel, R., Schultz-Johanning, M., & Kock, M. 2004, A&A, 414, 1169
Schönrich, R., Binney, J., & Dehnen, W. 2010, MNRAS, 403, 1829
Sestito, F., Longeard, N., Martin, N. F., et al. 2019, MNRAS, 484, 2166
Sitnova, T. M., Mashonkina, L. I., Ezzeddine, R., & Frebel, A. 2019, MNRAS, 485, 3527
Smiljanic, R., Pasquini, L., Bonifacio, P., et al. 2009, A&A, 499, 103
Speagle, J. S. 2020, MNRAS, 493, 3132
Spite, M., Bonifacio, P., Spite, F., et al. 2019, A&A, 624, A44
Spite, M., Cayrel, R., Hill, V., et al. 2006, A&A, 455, 291
Starkenburg, E., Aguado, D. S., Bonifacio, P., et al. 2018, MNRAS, 481, 3838
Takeda, Y., Hashimoto, O., Taguchi, H., et al. 2005, PASJ, 57, 751
Tauris, T. M. & van den Heuvel, E. P. J. 2006, in Compact stellar X-ray sources, Vol. 39, 623–665
Thomas, D., Schramm, D. N., Olive, K. A., et al. 1994, ApJ, 430, 291
Yong, D., Norris, J. E., Bessell, M. S., et al. 2013, ApJ, 762, 26

[1] LIRA, Observatoire de Paris, Université PSL, Sorbonne Université, Université Paris Cité, CY Cergy Paris Université, CNRS,92190 Meudon, France
[2] INAF-OATS, Via G.B.Tiepolo 11, Trieste, I 34143, Italy
[3] Leibniz-Institut für Astrophysik (AIP), An der Sternwarte 16, 14482 Potsdam, Germany
[4] Institute for Fundamental Physics of the Universe (IFPU), Via Beirut 2, I34151 Grignano, Trieste, Italy.
[5] Zentrum für Astronomie der Universität Heidelberg, Landessternwarte, Königstuhl 12, 69117 Heidelberg, Germany
[6] Instituto de Astrofísica de Canarias, Vía Láctea, 38205 La Laguna, Tenerife, Spain
[7] Universidad de La Laguna, Departamento de Astrofísica, 38206 La Laguna, Tenerife, Spain
[8] Centro de Astrobiología (CSIC-INTA), Carretera Ajalvir km 4, 28850 Torrejón de Ardoz, Madrid, Spain
[9] Universidad Andres Bello, Facultad de Ciencias Exactas, Departamento de Física y Astronomía – Instituto de Astrofísica, Autopista Concepción-Talcahuano 7100, Talcahuano, Chile
[10] Istituto Nazionale di Astrofisica - Osservatorio Astronomico di Roma (INAF - OAR), Via Frascati 33, I-00040, Monteporzio Catone, Italy
[11] Istituto Nazionale di Fisica Nucleare - Sezione di Perugia (INFN), via A. Pascoli s/n, I-06125 Perugia, Italy
[12] Kavli Institute for the Physics and Mathematics of the Universe, Todai Institutes for Advanced Study, University of Tokyo, Kashiwa, 277-8583 (Kavli IPMU, WPI), Japan
[13] Istituto Nazionale di Astrofisica - Istituto di Astrofisica e Planetologia Spaziali (INAF - IAPS), Via Fosso del Cavaliere 100, I-00133, Roma, Italy
[14] Monash Centre for Astrophysics (MoCA), School of Mathematical Sciences, Monash University, Victoria 3800, Australia
[15] Dipartimento di Fisica, Sapienza Università di Roma, P.le A. Moro 5, Roma 00185, Italy
[16] Istituto Nazionale di Fisica Nucleare - Laboratori Nazionali del Sud (INFN - LNS), Via Santa Sofia 62, Catania, Italy
[17] Konkoly Observatory, Research Centre for Astronomy and Earth Sciences, Eötvös Loránd Research Network (ELKH), Konkoly Thege Miklós út 15-17, H-1121 Budapest, Hungary
[18] CSFK, MTA Centre of Excellence, Konkoly Thege Miklós út 15-17, H-1121, Budapest, Hungary
[19] Goethe University Frankfurt, Institute for Applied Physics (IAP), Max-von-Laue-Str. 12, 60438 Frankfurt am Main, Germany
[20] UPJV, Université de Picardie Jules Verne, 33 rue St Leu, 80080 Amiens, France
[21] European Southern Observatory, Casilla 19001, Santiago, Chile
[22] Instituto de Astrofísica e Ciências do Espaço, Universidade do Porto, CAUP, Rua das Estrelas, 4150-762 Porto, Portugal
[23] Centro de Astrofísica da Universidade do Porto, Rua das Estrelas, 4150-762 Porto, Portugal
[24] Centre for Astrophysics and Supercomputing, Swinburne University of Technology, Hawthorn, Victoria 3122, Australia
[25] Instituto de Astrofísica e Ciências do Espaço, Faculdade de Ciências da Universidade de Lisboa, Campo Grande, PT1749-016 Lisboa, Portugal
[26] Departamento de Física e Astronomia, Faculdade de Ciências, Universidade do Porto, Rua do Campo Alegre, 4169-007 Porto, Portugal
[27] Observatoire Astronomique de l'Université de Genève, Chemin Pegasi 51, Sauverny, CH-1290, Switzerland

Appendix A: Data from the literature

The abundances and upper limits derived in the literture are reported in Table A.1, while in Table A.2 our results are listed.

Appendix B: Model atmospheres and spectrum synthesis

B.1. 1D (LTE) models and spectrum synthesis

As 1D model atmosphere we computed an ATLAS 9 (Kurucz 2005) model with $T_{\rm eff}$= 5100 K and log g 2.2, with metallicity [M/H]=−5.0, α enhancement +0.4 dex and microturbulence 1.0 $\rm kms^{-1}$, using the Opacity Distribution Function of Mucciarelli et al. (in preparation). The effect of microturbulence on the model structure and emerging flux is minor (see Kučinskas et al. 2018). The ODF used assumes the (scaled) solar abundances of Caffau et al. (2011b) and Lodders et al. (2009) for the elements not included in the former paper. This is also the set of solar abundances assumed elsewhere in this work.

We also computed an ATLAS 12 model atmosphere with the precise chemical composition of HE 0107−5240. We verified that the ATLAS 9 and ATLAS 12 models have exactly the same temperature structure for all layers that are relevant for the line formation. The two models begin to differ for $\log(\tau_{\rm Ross}) < -4$, the ATLAS 12 model being cooler. This difference is not due to the different chemical composition but is due to the different temperature correction algorithm in the two codes. One should bear in mind that real stars are expected to show a chromospheric temperature rise at very low optical depths that cannot be modelled by the 1D LTE approach of the ATLAS codes. We typically compute models up to optical depth of $\log(\tau_{\rm Ross}) \sim -6.5$ just to avoid an edge effect when computing the cores of strong lines. We do not claim that these are correctly computed, since they certainly are sensitive to the structure of the chromosphere and NLTE effects.

When computing the ATLAS models we used the default control card `SCATTERING ON` that includes the scattering term in the computation of the continuum source function. The effect of scattering is discussed in Bonifacio et al. (2018, section 2.3).

To compute the synthetic spectra from our 1D model atmosphere we used the SYNTHE suite (Kurucz 2005). The scattering is treated explicitly and without approximation. In fact, this is specially important in the UV range: if one does not treat scattering explicitly one finds a trend of abundances with wavelength (see Cayrel et al. 2004, section 3.2 for a discussion).

B.2. 3D (LTE) models and abundance corrections

Two dedicated high-resolution CO5BOLD models (288 × 288 × 200 grid) have been computed to represent the dynamic atmosphere of HE 0107–5240 ($T_{\rm eff}$ ∼ 5100 K, log g = 2.2). For the first model, we assumed [M/H]=−4.0 solar scaled abundances (with an α enhancement of +0.4 dex), for the second one an enhancement of C and N by 3.0 dex and of O by 2.6 dex was applied with respect to the first model. The detailed chemical composition is relevant for constructing the 14-band opacity tables used for computing the radiation transport in CO5BOLD. Continuum scattering is treated approximately by ignoring the scattering opacity in the optically thin layers as suggested by Collet et al. (2011), (see also Ludwig & Steffen 2012, 2013).

As shown in Fig. B.1, both models are characterised by substantial photospheric temperature fluctuations that cannot be captured by 1D (or 3D-averaged) models.[8] Spectral lines emerging from an inhomogeneous atmosphere can have a significantly different strength (an shape) compared to the same lines formed in a representative 1D (<3D>) atmosphere. In the present case, the investigated CH, NH, OH molecular lines show a highly nonlinear temperature dependence. The strong temperature fluctuations in the 3D models lead to a substantial enhancement of these lines, so that the abundances derived from these models are significantly lower than those obtained from a standard 1D analysis.

We use the line formation code Linfor3D[9] to compute synthetic spectra from selected snapshots of the 3D hydrodynamical model as well as from the 1D LHD reference model atmo-

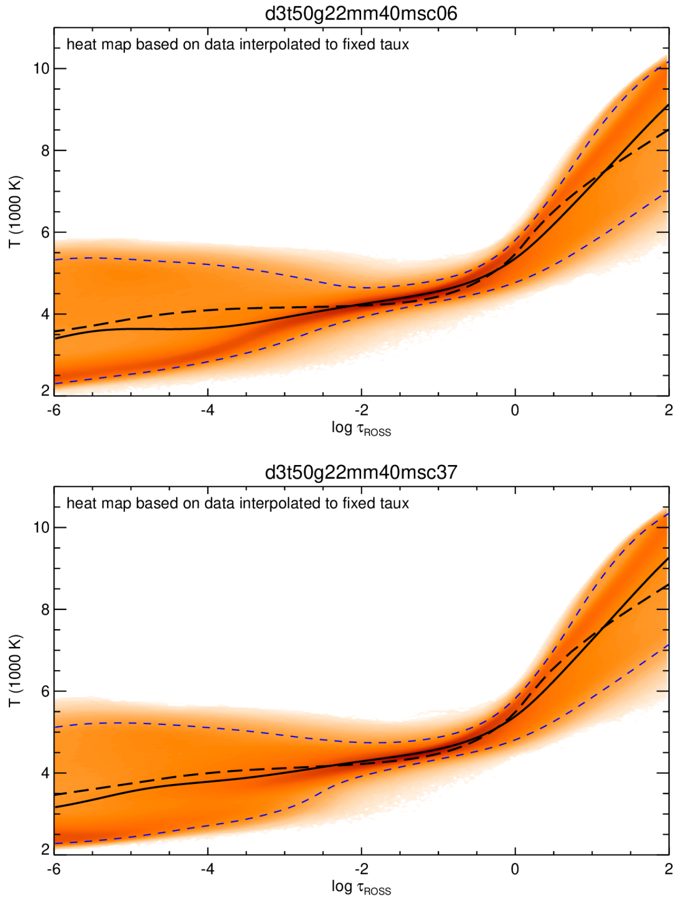

Fig. B.1. 3D versus 1D temperature structure of two 3D CO5BOLD models representing HE 0107–5240 ($T_{\rm eff}$ ∼ 5090 K, log g = 2.2, [M/H]=-4.0, α enhancement +0.4), assuming different CNO abundances for computing the opacity tables: *Top*: A(C)=4.39, A (N)=3.78, A(O)=5.06; *Bottom*: A(C)=7.39, A(N)=6.78, A(O)=7.66. The orange band outlines the 3D temperature distribution constructed from 20 snapshots of the respective high-resolution model, each resampled to 144 × 144 × 200 grid points. The dashed blue lines enclose 95, 5% of the data points at given Rosseland optical depth. The black solid line shows the <3D> model (the temperature of the 3D model averaged at constant $\tau_{\rm Ross}$), the black long-dashed line represents the $T(\tau_{\rm Ross})$ relation of the 1D LHD reference model atmosphere with identical stellar parameters, treating convection by standard mixing-length theory, but otherwise using the same input physics as the 3D hydrodynamical model.

[8] This is in stark contrast to the 3D temperature structure of SDSS J102915.14+172927.9, one of the most metal-poor star known to date, where horizontal temperature fluctuations are effectively suppressed (see Caffau et al. 2024b, Figure 2).

[9] `https://www.aip.de/en/members/matthias-steffen/linfor3d-user-manual/`

Table A.1. Abundances from the literature.

Element	NC02	NC04	B04	RC06	Y13	E17	S19	A22	M23
	[X/Fe]	A(X)					C-NLTE[1]		
$T_{\rm eff}$	5100	5100	5100	5130	5100	5050	5300	5100	5100
log g	2.2	2.2	2.2	2.2	2.2	2.3	2.5	2.2	2.2
Li	< 5.3	< 1.12		< 0.94				< 0.50	
C	4.0	6.81/7.11[2]		∼ 5.7[3]	6.74			6.90	6.75
12C/13C		∼ 60						87	
N	2.3	4.93/5.22[4]		∼ 3[5]	4.72			5.00	
O			5.66	∼ 5[6]					
Na	0.8	1.86		1.75	1.81			1.62	
Mg	0.2	2.41		2.33	2.32		0.30	2.24	
Al		< 0.93		< 0.79				< 0.90	
Si		< 2.55		< 2.45					
S		< 7.11		< 7.15					
K								< 1.22	
CaI	0.4	0.99		0.84	0.92		0.02	0.78	
CaII		1.44		1.24				1.43	
Sc		< −1.50		< −1.63					
Ti	−0.4	−0.62		−0.66	−0.55				
Cr		< 0.65		< 0.36				< 0.67	
Mn		< 0.47		< 0.08					
FeI	−5.3 ± 0.2	2.06/2.17[7]		1.83	1.96	2.03 ± 0.20/2.78 ± 0.15[7]		1.96	
FeII		< 3.00		< 3.06					
Co		< 0.86		< 0.60					
Ni	−0.4	0.60		0.27					
Zn	< 2.7	< 1.97		< 2.02					
Sr	< −0.5	< −2.83		< −3.00	< −3.19			< −3.40	
Ba	< 0.8	< −2.33		< −2.59	< −2.54			< −2.87	< −3.19
Eu	< 2.8	< −1.99		< −2.52					

NC02: Christlieb et al. (2002); NC04: Christlieb et al. (2004); B04: Bessell et al. (2004); RC06: Collet et al. (2006); Y13: Yong et al. (2013); E17: Ezzeddine et al. (2017); S19: Sitnova et al. (2019); A22: Aguado et al. (2022); M23: Molaro et al. (2023).
[1] NLTE corrections.
[2] From CH and C2 lines, respectively.
[3] average assuming two different A(C) of 7.11 and 6.81, respectively and on different lines.
[4] consistent values from CH and C2 lines.
[5] from CN lines.
[6] average value after 3D correction of several synthetic OH lines.
[7] LTE and NLTE.

sphere with identical stellar parameters and input physics as the 3D hydrodynamical model, except that convection is treated by the mixing-length theory. Linfor3D treats continuum scattering as true absorption which may compromise the synthetic spectra in the UV, e.g., of the OH lines near 319, 5 nm. However, the abundance corrections are probably affected only marginally since the same scattering approximation is used for the line formation in the 3D and the 1D LHD models.

3D abundance corrections are derived for individual spectral lines from a comparison of 3D and 1D equivalent widths. More specifically, if the observed equivalent width of a spectral line of element X is reproduced with (logarithmic) abundance $A_{\rm 3D}(X)$ based on the 3D model and with $A_{\rm 1D}(X)$ when using the 1D model, the 3D abundance correction is defined as $\Delta_{\rm 3D} = A_{\rm 3D}(X) - A_{\rm 1D}(X)$. For the molecular lines and the Fe II line investigated in this work, both 3D and 1D line formation are treated in LTE.

It must be noted that the 3D abundance correction of partly saturated lines depends on the microturbulence velocity assumed in the 1D spectrum synthesis. Here we have determined the optimal value of the microturbulence as 1.3 km s^{-1} from a curve-of-growth analysis of the Fe II line at 516.9 nm.

In the present work, the ^{12}C/^{13}C isotopic ratio is derived from the CH lines in the G-band where the ^{12}CH and the ^{13}CH lines are well separated such that their individual equivalent widths can be measured. We can therefore compute individual 3D abundance corrections, $\Delta^{12}_{\rm 3D}$ and $\Delta^{13}_{\rm 3D}$ for both isotopic components as described above. The isotopic ratio derived in 3D, $q_{\rm 3D}$, is related to the 1D isotopic ratio, $q_{\rm 1D}$, by $\log(q_{\rm 3D}/q_{\rm 1D}) = \Delta^{12}_{\rm 3D} - \Delta^{13}_{\rm 3D}$. If the corrections for both components are identical, the 3D correction factor for the isotopic ratio is $R_q = q_{\rm 3D}/q_{\rm 1D} = 1$.

As mentioned in Sect. 5.3, the magnitude of the 3D corrections depends on the chemical composition, in particular the CNO abundances, adopted for the construction of the 3D atmosphere and the 1D reference model. This is because the molecular opacities influence the resulting temperature structure, as demonstrated in Fig. B.1. The model with the lower CNO abundances (model A, top panel) shows a T-distribution that is strongly biased towards the lowest temperatures, visible as the dark-orange band in the upper photosphere, which leads to a

Table A.2. Abundances derived in this work.

Element	A(X)$_\odot$	A(X)	[X/H]	[X/Fe]	3D LTE corr
Fe I$^{(*)}$	7.52	1.96	−5.56		
Be I	1.38	< −2.05	< −3.44	< 2.12	
Li I	1.03	< −0.14			
^{12}C I		6.72			−0.65
^{13}C I		4.68			
N I	7.86	4.42	−3.44	+2.12	−0.58
O I	8.76	5.72	−3.04	+2.52	−0.58
Na I	6.30	1.64	−4.66	0.90	
Al I	6.47	0.27 :	−6.20 :	−0.64 :	
Si I	7.52	< 1.8	< −5.72	< −0.16	
S I	7.16	< 4.40	< −2.76	< 2.80	
K I	5.11	< 1.05	< −4.06	< 1.56	
Sc II	3.10	−2.30	−5.40	0.16	
Cr I	5.64	< 0.30	< −5.34	< 0.22	
Mn I	5.26	< −0.50	< −5.76	< −0.20	
Fe II	7.52	1.74			+0.10
Co I	4.92	0.30 :	−4.62 :	+0.94 :	
Zn I	4.62	< 1.02	< −3.60	< 1.96	
Sr II	2.92	< −3.89	< −6.81	< −1.25	
Ba II	2.17	< −3.87	< −6.04	< −0.48	
Eu II	0.51	< −2.67	< −3.18	< 2.38	

$^{(*)}$ A(Fe) is from Aguado et al. (2022) and it is used in the table for [Fe/H] to compute [X/Fe] for all the elements.

plateau in the <3D> temperature profile around log $\tau_{\rm Ross} \sim -4$. In the model with enhanced CNO abundances (model B, bottom), the T-distribution is more symmetric, and the <3D> and 1D $T(\tau)$ relations are more similar throughout the photosphere.

The physical reasons for these differences need yet to be understood. For given carbon abundance, model A produces stronger CH lines due to the excess of cool temperatures. It appears plausible that the larger asymmetry of the T-distribution and the larger separation between <3D> and 1D reference model lead to larger (more negative) 3D abundance corrections for the molecular lines in model A than in model B. Since the 3D and 1D curves-of-growth are running almost parallel in model B, the correction factor for the isotopic ratio is close to 1, while it is significantly below 1 in model A.

Reliable 3D corrections can only be evaluated when a new 3D model is available that is based on a (yet unavailable) custom-made opacity table representative of the actual chemical composition of HE 0107–5240.

Appendix C: Ionised Fe in SMSS J160540.18–144323.1

The problem, discussed in Sec. 6.1.2, about the large NLTE corrections for HE 0107−5240 proposed in the literature for A(Fe) from Fe I lines (see Ezzeddine et al. 2017; Nordlander et al. 2017) and that bring tension with A(Fe) from Fe II lines, is also true for SMSS J160540.18–144323.1 (Nordlander et al. 2019). We took the advantage of 18 ESPRESSO observations to investigate the Fe II line at 516.9 nm, the same one investigated in HE 0107−5240 and shown in the lower panel of Fig. 8. We here suppose that the NLTE correction for Fe II line is negligible for this star as for HE 0107−5240. In Fig. C.1 the observed spectrum of SMSS J160540.18–144323.1 (solid black) is compared to a synthesis (solid blue) with the LTE iron abundance derived

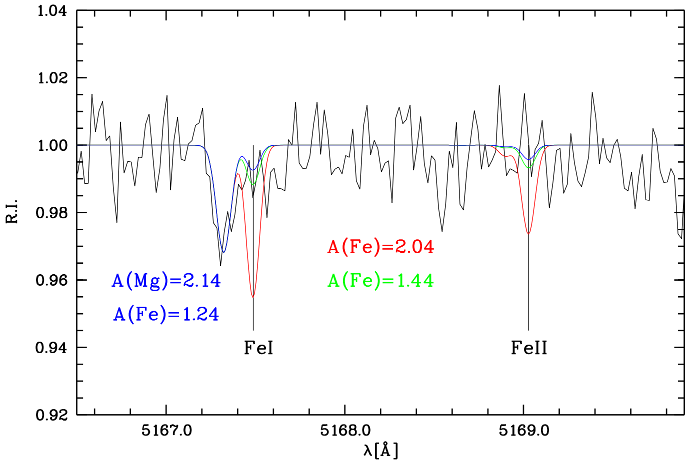

Fig. C.1. Observed spectra (solid black) of SMSS J160540.18–144323.1, compared to 1D-LTE synthesis with different A(Fe) values (solid blue, green and red).

from neutral Fe lines (A(Fe)=1.24 Nordlander et al. 2019): the agreement observation/synthesis is good for both the Fe I and the Fe II line, which is not detected. A NLTE correction of +0.2 dex in Fe I (a value compatible with the NLTE correction for a more metal rich model derived in the MPIA database and discussed in Sec. 5.3) would bring A(Fe)=1.44: the solid green synthesis in the figure shows that the profile is compatible with the observations of the Fe II line. The 'large' NLTE correction on Fe I (as suggested by Nordlander et al. 2017; Ezzeddine et al. 2017) is not compatible with the observation. A NLTE correction of +0.8 dex would bring the LTE A(Fe) value at 2.04, and this is shown as a red solid profile in the figure. Clearly such a NLTE correction would imply the Fe II line to be visible at this observation quality, and this is not the case. A dedicated work will perform a careful investigation of this line as well as a complete analysis of this ESPRESSO spectrum.